UNIVERSITY OF LEEDS

This is a repository copy of *Efficient Visual Computing with Camera RAW Snapshots*.

White Rose Research Online URL for this paper:
https://eprints.whiterose.ac.uk/208499/

Version: Accepted Version

Article:
Li, Z. orcid.org/0000-0002-2066-8775, Lu, M. orcid.org/0000-0002-5044-8802, Zhang, X. orcid.org/0000-0002-1882-736X et al. (3 more authors) (2024) Efficient Visual Computing with Camera RAW Snapshots. IEEE Transactions on Pattern Analysis and Machine Intelligence. ISSN 0162-8828

https://doi.org/10.1109/tpami.2024.3359326

© 2024 IEEE. Personal use of this material is permitted. Permission from IEEE must be obtained for all other uses, in any current or future media, including reprinting/republishing this material for advertising or promotional purposes, creating new collective works, for resale or redistribution to servers or lists, or reuse of any copyrighted component of this work in other works.

Reuse
Items deposited in White Rose Research Online are protected by copyright, with all rights reserved unless indicated otherwise. They may be downloaded and/or printed for private study, or other acts as permitted by national copyright laws. The publisher or other rights holders may allow further reproduction and re-use of the full text version. This is indicated by the licence information on the White Rose Research Online record for the item.

Takedown
If you consider content in White Rose Research Online to be in breach of UK law, please notify us by emailing eprints@whiterose.ac.uk including the URL of the record and the reason for the withdrawal request.

White Rose university consortium
Universities of Leeds, Sheffield & York

eprints@whiterose.ac.uk
https://eprints.whiterose.ac.uk/

Efficient Visual Computing with Camera RAW Snapshots

Zhihao Li, Ming Lu, Xu Zhang, Xin Feng, M. Salman Asif, and Zhan Ma

Abstract—Conventional cameras capture image irradiance (RAW) on a sensor and convert it to RGB images using an image signal processor (ISP). The images can then be used for photography or visual computing tasks in a variety of applications, such as public safety surveillance and autonomous driving. One can argue that since RAW images contain all the captured information, the conversion of RAW to RGB using an ISP is not necessary for visual computing. In this paper, we propose a novel ρ-Vision framework to perform high-level semantic understanding and low-level compression using RAW images without the ISP subsystem used for decades. Considering the scarcity of available RAW image datasets, we first develop an unpaired CycleR2R network based on unsupervised CycleGAN to train modular unrolled ISP and inverse ISP (invISP) models using unpaired RAW and RGB images. We can then flexibly generate simulated RAW images (simRAW) using any existing RGB image dataset and finetune different models originally trained in the RGB domain to process real-world camera RAW images. We demonstrate object detection and image compression capabilities in RAW-domain using RAW-domain YOLOv3 and RAW image compressor (RIC) on camera snapshots. Quantitative results reveal that RAW-domain task inference provides better detection accuracy and compression efficiency compared to that in the RGB domain. Furthermore, the proposed ρ-Vision generalizes across various camera sensors and different task-specific models. An added benefit of employing the ρ-Vision is the elimination of the need for ISP, leading to potential reductions in computations and processing times.

Index Terms—Camera RAW, RAW-domain Object Detection, RAW Image Compression

arXiv:2212.07778v2 [cs.CV] 25 Jan 2024

1 Introduction

Conventional cameras capture visual information in a scene and present it in the RGB (or equivalent YCbCr) format for subsequent visual computing (e.g., semantic understanding and communication). This pipeline is prevalent in a variety of applications [1]–[3], such as smart communities [4], and surveillance systems [5]. For instance, instantaneous RGB snapshots enable the detection of driving lanes or pedestrians in advanced driver assistance systems [6] to improve road safety and risk prevention.

The camera sensor and image signal processor (ISP) are tightly coupled for traditional RGB-Vision, as illustrated in Fig. 1a. First, a CMOS or CCD sensor records color pixels in a Bayer pattern as a RAW image. Then, an ISP converts the RAW image to RGB representation through a series of linear and nonlinear steps (e.g., demosaicing, white balance, exposure control, gamma correction, and JPEG compression) [7]. The compressed RGB images are then processed for various vision tasks and potentially stored for archival or review purposes.

The classic RGB-Vision pipeline used in cameras for decades has significant redundancies. As for the surveillance video usage reported by leading video hosting firms, less than $1\,\%$ of recorded videos are reviewed by human subjects [8]. The transformation process of the ISP is not just resource-intensive with additional hundreds of mW power consumption [9]—but also introduces additional processing delays. These delays are particularly detrimental in latency-sensitive applications, such as autonomous vehicles. Moreover, domain discrepancy is inevitable if we train and test models using RGB images generated from different ISPs, adversely affecting the inference accuracy[1]. This raises a question *why do we need the ISP to convert RAW images to the human-perceivable RGB format?*

In this work, we present a ρ-Vision framework[2] to execute both high-level and low-level tasks directly on camera RAW images. The key steps of ρ-Vision pipeline are illustrated in Fig. 1b. As an increasing number of artificial intelligence (AI) chips are installed on cameras [10], it is feasible to utilize in-camera AI chips for RAW image processing in various tasks.

One fundamental challenge in developing models for RAW-domain visual computing is the *lack sufficient RAW images and task-associated label annotations to train robust RAW-domain models*, since existing models are mainly developed for the RGB domain, large-scale, publicly accessible datasets consisting of RGB images (e.g., ImageNet [11]). On the other

This paper is supported in part by the National Natural Science Foundation of China (62022038, U20A20184, 62171174), the Key project of Natural Science Foundation of Chongqing, China under Grant No.CSTB2022NSCQ-MSX0493, Chongqing Technology Innovation and Application Development under Grant No.cstc2021jscx-dxwtBX0018. (Corresponding authors: Z. Ma and X. Feng.)

Z. Li, M. Lu, and Z. Ma are with the School of Electronic Science and Engineering, Nanjing University, Nanjing, Jiangsu, China. M. Lu is also with the Interdisciplinary Research Center for Future Intelligent Chips (Chip-X), Nanjing University, Suzhou, Jiangsu, China. E-mails: lizhihao6@smail.nju.edu.cn, {minglu, mazhan}@nju.edu.cn

X. Zhang is with the University of Leeds, Leeds LS2 9JT, United Kingdom. Email: x.zhang15@leeds.ac.uk

X. Feng is with the Chongqing University of Technology, Chongqing, China. Email: xfeng@cqut.edu.cn

M. S. Asif is with the University of California Riverside, CA 92521. Email: sasif@ece.ucr.edu

1. Due to the space limitation, more details about this real-world experiment using commodity hardware are provided in the supplementary material.

2. Greek letter ρ represents the "RAW" for similar pronunciation.

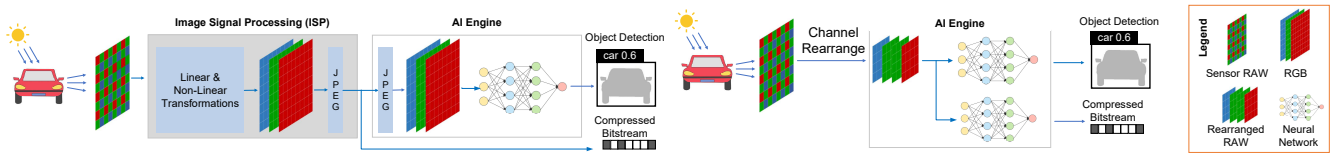

(a) Traditional RGB-Vision pipeline

(b) The proposed ρ-Vision framework

Fig. 1: **Cameras for visual computing tasks.** (a) Traditional RGB-Vision framework (with in-camera ISP) executes tasks with RGB images; (b) Proposed ρ-Vision framework (without conventional ISP) executes with RAW images directly.

hand, directly applying pre-trained RGB-domain models to RAW images can lead to catastrophic performance degradation (see Table 2).

To address the challenges posed by dataset limitations, we developed the Unpaired CycleR2R model. This model leverages existing RGB images to generate simulated RAW (simRAW) images. These simRAW images are produced using inverse ISP (invISP) methods, with which fine-tuning the existing RGB-domain models for RAW-domain tasks with uncompromised performance is assured. Training the Unpaired CycleR2R does not require paired RGB and RAW images. Instead, we can use the existing large-scale RGB dataset (e.g., 100,000 samples) and a much smaller RAW dataset (e.g., 7,000 images) to fulfill the purpose. This is particularly valuable given the challenges and high costs of acquiring a large-scale RAW image dataset (samples and label annotations). The Unpaired CycleR2R not only transforms the existing RGB dataset to its RAW-domain counterpart but also allows us to reuse its labels for subsequent task models directly, completely avoiding the tedious and expensive labeling. We then run a RAW-domain YOLOv3 to process RAW images, reporting better detection accuracy than the corresponding RGB-domain YOLOv3 used in several applications [12]. We also extend a variational autoencoder (VAE) based lossy/lossless RAW Image Compressor (RIC) from the TinyLIC [13] for RAW image compression. The resulting model shows superior performance to commercial approaches in both lossy and lossless modes.

This paper makes the following contributions:

1) **Unpaired CycleR2R** for conversion between RAW and RGB images. We train a CycleGAN to train an ISP for RAW-to-RGB and an invISP for RGB-to-RAW transformation (R2R) using unpaired RGB and RAW images. Unsupervised learning using unpaired samples makes our approach much more accessible for practical implementation. In contrast, existing solutions (e.g., CycleISP [14], CIE-XYZ Net [15], and MBISPLD [16]) are supervised models that require paired RAW and RGB images (from the same camera model).
   - Instead of training a generic deep network for ISP and invISP, we apply the modular unrolling to mimic functional steps in ISP and invISP subsystems, to which each step is motivated by imaging physics.
   - Since the same scene can be mapped into the different RAW samples by setting different brightness and color temperature levels, we characterize the probabilistic distribution of the illumination instead of using a fixed setting to best represent the practical conditions for the modeling of invISP/ISP.
2) **RAW-domain models** (in principle) can be obtained by retraining corresponding RGB-domain models using the simRAW images generated using the proposed invISP. Such domain adaptation approaches [17]–[19] need to be separately engineered for each individual task.
   - In our experiments, we demonstrate that YOLOv3 and RIC finetuned using simRAW samples provide outstanding performance for object detection and image compression in the RAW domain. We can consistently enhance their performance by further finetuning simRAW-tuned models with limited real RAW images from various camera models. Such a lightweight, few-shot fine-tuning method generalizes our method for camera-specific RAW-domain processing, which is attractive for practitioners.
   - To encourage the reproducible research, a labeled MultiRAW dataset that contains >7k RAW images acquired using multiple camera sensors is made publicly accessible for RAW-domain processing.

2 Related Work

This section briefly reviews relevant approaches for camera ISP, RAW image processing, and simRAW generation.

2.1 Camera ISP

Modern ISP converts sensor RAW data to RGB images using a series of computations, as shown in Fig. 1a. First, linear transformations, including demosaicing, white balance estimation, brightness adjustment, and color correction, are applied to map native RAW input to an intermediate format conforming to the CIE 1931 XYZ color space [20]. Subsequently, a sequence of nonlinear transformations translates the image from XYZ to RGB color space. Typical nonlinear operations include gamma correction and local transformations (e.g., denoising, sharpening, local tone mapping). Then, a JPEG encoder is used to compress the RGB images for storage or transmission. The entire processing pipeline of such ISP subsystems is widely used in commodity cameras. A white paper on the ISP system can be found here [21]. To summarize, the ISP mainly converts sensor RAW samples to human-perceivable RGB images, which induces redundant computations, as discussed earlier.

2.2 RAW Image Processing

Although most image processing algorithms have been developed for RGB images, recent explorations on RAW images have revealed superior performance for various tasks

(e.g., denoising, deblurring) [14], [16], [22]. For instance, Brooks *et al*. [23] applied the UPI, Zamir *et al*. [14] proposed a CycleISP, Conde *et al*. [16] developed a learned dictionary-based model to convert an RGB image to its RAW format for denoising.

One challenge with processing RAW images is their strong dependence on specific sensors and devices, which makes the aforementioned methods difficult to generalize to multiple sensors. Afifi *et al*. [15] suggested processing images in device-independent CIE XYZ format that could be easily mapped from the sensor-specific RAW image via a colorimetric conversion. They not only reported performance improvement for various low-level tasks (e.g., denoising, deblurring, and defocusing) but also demonstrated the model generalization without requiring per-sensor supervision.

Existing works mainly focus on the low-level processing of RAW images. In this paper, we explore high-level semantic understanding tasks (e.g., object detection and segmentation). We also investigate low-level RAW image compression (RIC) for two reasons: 1) RIC is a commodity feature vastly used in cameras to ensure efficient storage and exchange of image snapshots; 2) the studies of denoising and deblurring in [14]–[16], [23] can be easily extended in our framework. To the best of our knowledge, this work, together with our earlier work in [24] offers the first study on the lossy and lossless compression of RAW images.

2.3 simRAW Generation

RAW-domain visual computing has promising prospects, as demonstrated by existing work, but training large neural networks for RAW-Vision requires large annotated datasets with RAW images. Collecting RAW images is somewhat easy and straightforward. However, the associated annotation labeling in the RAW domain is expensive and burdensome. Also, when we refer to a dataset used for the vision task, we generally assume the composite of the image samples and their label annotations. Thus, one approach is to generate RAW images from prevalent labeled RGB datasets, which requires reverse engineering the ISP, which we call invISP. Earlier algorithms, such as InvGamma [25], assume the availability of spectral characterization of a target camera to train the reverse imaging pipeline. Recently, CycleISP [14] and CIE-XYZ Net [15] suggested learning invISP module by fully leveraging the nonlinear representative capacity of underlying deep neural networks (DNNs). Training such models requires a large number of paired RAW and RGB images (e.g., DND dataset used by CycleISP [26] and MIT-Adobe FiveK [27] used in CIE-XYZ Net).

DNNs trained to characterize invISP (and ISP, if applicable) are hardly interpretable. Brooks *et al*. [23] (UPI) and Conde *et al*. [16] (MBISPLD) applied algorithm unrolling [28] to model modular components in the ISP subsystem by leveraging imaging physics. Such modular unrolling-based approaches were expected to require a small number of sample pairs for training [16]. Yet, UPI and MBISPLD still need paired RGB and RAW images, which limits the application in converting existing RGB datasets captured by unknown cameras, like BDD100K [29] into RAW format.

We propose the "Unpaired CycleR2R" to properly model the invISP and ISP functions. We not only follow the CycleGAN structure [17] to characterize the mapping functions using unpaired RAW (instantaneously captured by cameras) and RGB (obtained from existing datasets) images in an unsupervised manner but also enforce the modular unrolling approach for more robust model derivation. Though our method shares the general architecture of modular unrolling for invISP/ISP modeling with state-of-the-art MBISPLD [16], our method suggests the use of a probabilistic model to reflect non-bijective functional mapping in ISP modules. This is because the same RGB may come from a variety of RAWs acquired using different sensors or the same sensor with different illumination settings, while MBISPLD [16] strictly assumes the bijective mapping in the ISP subsystem.

3 Unpaired CycleR2R

This section presents details on how to easily simulate realistic RAW (simRAW) images from existing RGB image datasets.

3.1 Problem Definition and CycleGAN Approach

Existing work in [14], [15], [30] model the invISP process from RGB to RAW ($g : \mathcal{Y} \rightarrow \mathcal{X}$) as a one-to-one mapping in a supervised manner, for which a large number of paired RAW and RGB images (from the same camera) are required. Apparently, such a one-to-one mapping-based invISP does not reflect the imaging circumstances in practice. For example, the same scene may be acquired as two different RAW samples because of different illumination settings, but the resultant RGB image (after the ISP) would be the same because the camera ISP is capable of making a proper estimation of those settings for realistic rendering.

The proposed Unpaired CycleR2R learns a one-to-many mapping of invISP through the introduction of the iillumination estimation module (IEM) that provides a distribution of color temperature θ and brightness ϕ. Note that the use of unpaired RAW and RGB images avoids the collection of paired samples, making the solution more attractive and generally applicable in vast scenarios. Figure 2a provides an overview of the proposed Unpaired CycleR2R. We first use the IEM to estimate the illumination distribution of a scene. Then we sample a variety of θ and ϕ to simulate different illumination conditions used in practice (Sec. 3.2). These θ and ϕ are then used to generate various simRAW samples for a given RGB input (Sec. 3.3). We use a set of loss functions to guide the generation of realistic simRAW images (Sec. 3.4).

3.2 Illumination Estimation Module (IEM)

The same scene may appear differently in the RAW domain if different color temperature θ and brightness level ϕ are used in the acquisition. The ISP module estimates the θ and ϕ to generate properly-exposed RGB images under standard color temperature (D65 standard [31]). This suggests the one-to-many mappings from RGB to RAW and unknown values of θ and ϕ used in the camera make the invISP an ill-posed problem.

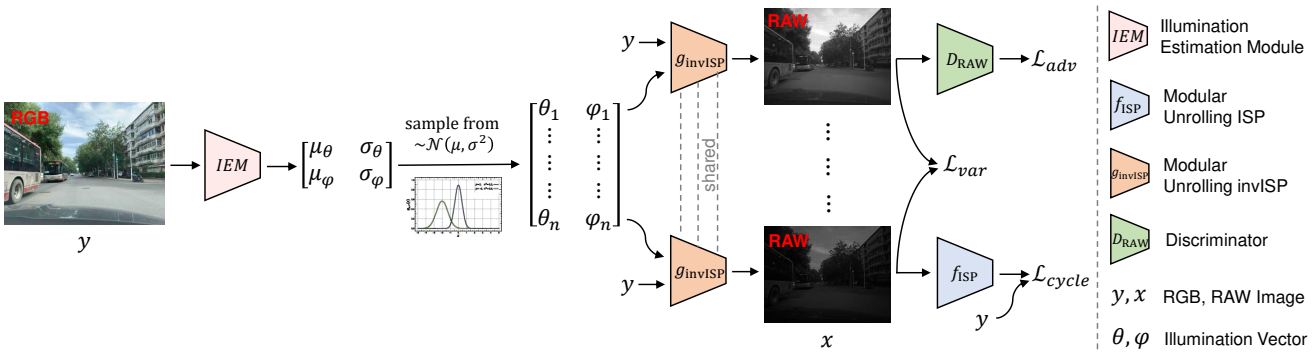

(a) Unpaired CycleR2R Framework.

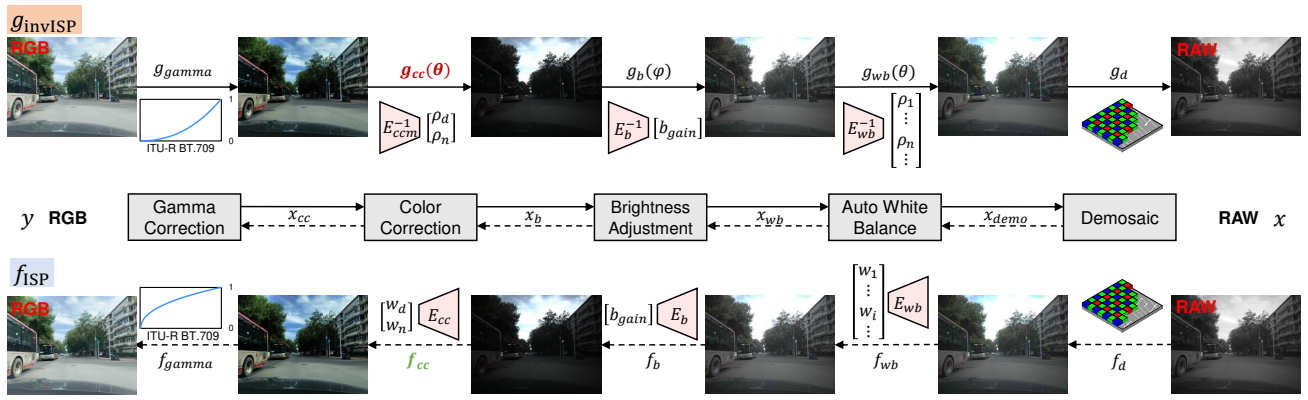

(b) Detail architectures of g_{invISP} and f_{ISP} .

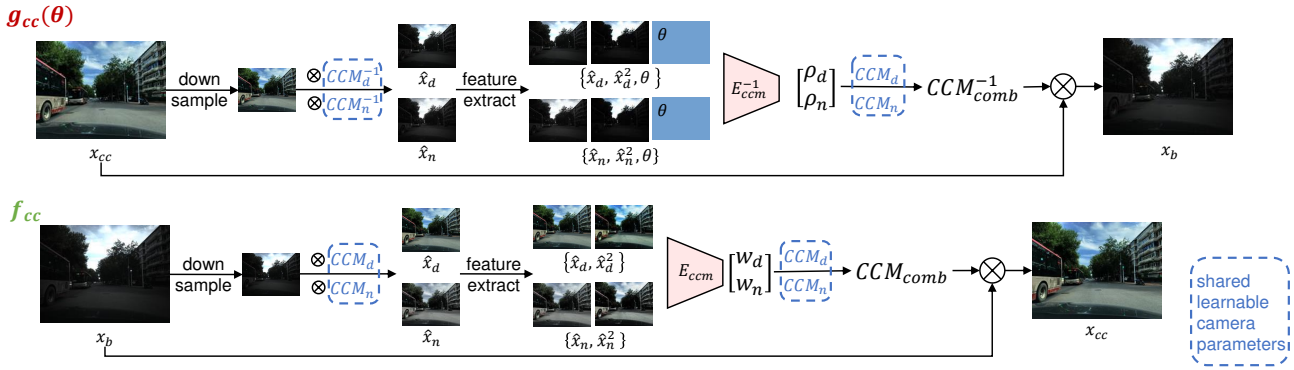

(c) Color correction f_{cc} and inverse $g_{cc}(\theta)$.

Fig. 2: **Unpaired CycleR2R.** (a) Our framework consists of an illumination estimation module (IEM) (Sec. 3.2), modular unrolling based ISP/invISP (Sec. 3.3) and unsupervised loss functions (Sec. 3.4). (b) The proposed framework simultaneously learns g_{invISP}: RGB $\rightarrow$ RAW, and f_{ISP}: RAW to $\rightarrow$ RGB with modular unrolling to best leverages the imaging physics in ISP/invISP for more robust model derivation. (c) Color correction f_{cc} in f_{ISP} and its inverse process $g_{cc}(\theta)$ in g_{invISP} are exemplified while other modules mostly follow the similar method.

To tackle the ill-posed problem, we propose the IEM to estimate the original θ and ϕ. We assume that the θ and ϕ follow the Gaussian distributions as $\mathcal{N}(\mu_\theta,\ \sigma_\theta)$ and $\mathcal{N}(\mu_\phi,\ \sigma_\phi)$ [32]. The IEM consists of three convolutional layers and two linear layers (see details in the supplemental material). During the training phase, the θ and ϕ are randomly sampled from Gaussian distribution and estimated through the guidance of $\mathcal{L}_{adv}$, $\mathcal{L}_{var}$ and $\mathcal{L}_{cycle}$ jointly to best simulate the real-world illumination.

3.3 Modeling of the ISP (invISP) via Modular Unrolling

Although it is possible to build a black box neural network to represent the ISP/invISP functions, an interpretable network design is preferred for robust inference and wide generalization [16], [28]. Therefore, we use modular unrolling to mimic the imaging physics involved in ISP and to build efficient $f_{\text{ISP}}/g_{\text{invISP}}$ used in the Unpaired CycleR2R framework.

Modern ISP systems in cameras are generally comprised of five major steps from RAW input to corresponding RGB output, as shown in Fig. 2b: demosaicing f_d, auto white

balance f_{wb}, brightness adjustment f_b, color correction f_{cc}, and gamma correction f_g. Thus the ISP function can be expressed as:

$$f_{\text{ISP}} = f_g \circ f_{cc} \circ f_b \circ f_{wb} \circ f_d, \tag{1}$$

$$\boldsymbol{y} = f_{\text{ISP}} \circ \boldsymbol{x}, \tag{2}$$

where $\boldsymbol{y} \in \mathcal{Y}$ denotes an RGB image, $\boldsymbol{x} \in \mathcal{X}$ denotes a RAW image, and $\circ$ denotes the function composition operation. The invISP mirrors each step with illumination prior $\theta,\ \phi$ as

$$g_{\text{invISP}} = g_d \circ g_{wb}(\theta) \circ g_b(\phi) \circ g_{cc}(\theta) \circ g_g, \tag{3}$$

$$\boldsymbol{x} = g_{\text{invISP}} \circ \boldsymbol{y}, \tag{4}$$

where we assume $g = f^{-1}$, for simplicity.

3.3.1 Demosaicing

Color (RGB) pixels on an image sensor are typically arranged in a Bayer pattern, half green, one-quarter red, and one-quarter blue (also called RGGB). To obtain a full-resolution color image, various demosaicing algorithms [33] have been developed in the past. For simplicity, we bilinearly upsample same-color pixels in close proximity to obtain demosaiced image $\boldsymbol{x}_{demo}$. Similarly, in invISP, we reverse the process to mosaic $\boldsymbol{x}_{demo}$ for its RAW output as

$$\boldsymbol{x}_{demo} = f_d \circ \boldsymbol{x}, \quad \boldsymbol{x} = g_d \circ \boldsymbol{x}_{demo}. \tag{5}$$

3.3.2 Auto White Balance (AWB)

Cameras apply the white balance to ensure color constancy, which requires accurate approximation of the color temperature. Practical solutions often achieve this by augmenting the digital gains in Red and Blue channels [23], [34]. For instance, various gain presets, $\{(R_{gain}, B_{gain})\}$ = $\{(r_1,\ b_1), \ldots, (r_N, b_N)\}$, can be defined for specific color temperatures. These presets are linearly weighted for auto white balance (AWB) because ambient illumination in real-life scenarios often mixes radiance from different light sources as

$$\begin{aligned}(r_{gain}, b_{gain}) &= W \cdot \{(R_{gain},\ B_{gain})\}^T \\ &= (\sum_{i=1}^{N} w_i r_i,\ \sum_{i=1}^{N} w_i b_i),\end{aligned} \tag{6}$$

where $W = \{w_1, \ldots, w_N\}$ is the weighting vector, and N is total number of gain presets. As seen, accurate AWB relies on the proper choice of the w_i, r_i and b_i in f_{wb} to derive $[r_{gain}, 1, b_{gain}]$ which is then multiplied with every pixel in the R, G, and B channels.

In general, the AWB function f_{wb} in ISP maps the demosaiced image $\boldsymbol{x}_{demo}$ into a white-balanced image $\boldsymbol{x}_{wb}$. Given that AWB adjusts the global appearance of the image, we downscale the native input $\boldsymbol{x}_{demo}$ to $\boldsymbol{x}^{\downarrow}_{demo}$ at a size of 128×128×3 for processing, with which we can significantly reduce the space and time complexity. Specifically,

- Starting with $\boldsymbol{x}^{\downarrow}_{demo}$, we generate a pre-AWB image $\hat{\boldsymbol{x}}_{wb_i}$ by multiplying every channel with a preset gain $[r_i, 1, b_i]$. In training, we randomly initialize r_i, and b_i following [23]. As suggested in [35], [36] for camera AWB or color correction, $\hat{\boldsymbol{x}}_{wb_i}$ is paired with $\hat{\boldsymbol{x}}^2_{wb_i}$ for learning.
- Then, we propose the $E_{wb}(\cdot)$ that shares the same architecture with IEM, but with one-channel output, to process $\{\hat{\boldsymbol{x}}_{wb_i},\ \hat{\boldsymbol{x}}^2_{wb_i}\}$ for weight derivation as

$$w_i = E_{wb}(\{\hat{\boldsymbol{x}}_{wb_i},\ \hat{\boldsymbol{x}}^2_{wb_i}\}), \tag{7}$$

  and subsequently the final AWB gain as in (6).
- Finally, instead of multiplying the AWB gain with every pixel of $\boldsymbol{x}_{demo}$ directly, highlight-preserving transformation $S(\boldsymbol{x},\ \texttt{scalingFactor})$ is applied to avoid highlight overflow [23] as

$$\boldsymbol{x}_{wb} = f_{wb} \circ \boldsymbol{x}_{demo} = S(\boldsymbol{x}_{demo},\ [r_{gain}, 1, b_{gain}]). \tag{8}$$

Correspondingly, for g_{wb} in invISP, we reverse engineer the f_{wb} to derive $[1/r_{gain},\ 1,\ 1/b_{gain}]$. As mentioned before, the original color temperature is unknown in g_{wb}. Therefore, we model the inverse weights $\{\rho_1, \ldots, \rho_N\}$ using E^{-1}_{wb} with the color temperature prior θ estimated by the IEM. Note that $E^{-1}_{wb}(\cdot)$ shares the same architecture with $E_{wb}(\cdot)$. The processing steps are as follows.

- Apply preset inverse gain on downscaled input $\boldsymbol{x}^{\downarrow}_{wb}$ as $\hat{\boldsymbol{x}}_{demo_i} = [1/r_i,\ 1,\ 1/b_i] \cdot \boldsymbol{x}^{\downarrow}_{wb}$.
- Derive the weight and inverse AWB gain as

$$\rho_i = E^{-1}_{wb}(\{\hat{\boldsymbol{x}}_{demo_i},\ \hat{\boldsymbol{x}}^2_{demo_i},\ \theta\}), \tag{9}$$

  and compute $(1/r_{gain},\ 1/b_{gain}) = \sum_i \rho_i \cdot (1/r_i,\ 1/b_i)$.
- Generate $\boldsymbol{x}_{demo}$ as

$$\boldsymbol{x}_{demo} = g_{wb}(\theta) \circ \boldsymbol{x}_{wb} = [\frac{1}{r_{gain}}, 1, \frac{1}{b_{gain}}] \cdot \boldsymbol{x}_{wb}. \tag{10}$$

Such derivations of w_i and ρ_i are also used in brightness adjustment and color correction to characterize the non-bijective mapping.

3.3.3 Brightness Adjustment (BA)

Existing ISPs usually adjust the brightness of overexposed or underexposed RAW images by enforcing range-limited global gain b_{gain} to scale every pixel uniformly [37]. We use a neural network $E_b(\cdot)$, which shares the same architecture as $E_{wb}(\cdot)$, to derive b_{gain}. We use a downscale and grayscale version of $\boldsymbol{x}_{wb}$, denoted as $\boldsymbol{x}^{\downarrow G}_{wb}$, because brightness adjustment is a global operation that does not require full-resolution spatial and spectral details.

We compute $b_{gain} = \beta + \alpha \cdot \tanh(E_b(\boldsymbol{x}^{\downarrow G}_{wb}))$, in the range of $[\beta - \alpha, \beta + \alpha]$ with α = 0.3 and β = 1, following the suggestions in [23]. Finally, we also apply highlight-preserving transformation $S(\cdot,\ \cdot)$ used in [23] to have $\boldsymbol{x}_b$:

$$\boldsymbol{x}_b = f_b \circ \boldsymbol{x}_{wb} = S(\boldsymbol{x}_{wb}, b_{gain}). \tag{11}$$

For g_b in invISP, we reverse the adjustment on well-exposed $\boldsymbol{x}_b$ using $1/b_{gain}$. Considering that a series of images captured in the same scene using different exposure levels could be rectified to the same well-exposed image after brightness adjustment, we introduce the brightness prior ϕ to recover $\boldsymbol{x}_{wb}$ as

$$b_{gain} = \beta + \alpha \cdot \tanh(E^{-1}_b(\{\boldsymbol{x}^{\downarrow G}_b, \phi\})). \tag{12}$$

We multiply $1/b_{gain}$ with $\boldsymbol{x}_b$ to generate $\boldsymbol{x}_{wb}$ as

$$\boldsymbol{x}_{wb} = g_b \circ \boldsymbol{x}_b = 1/b_{gain} \cdot \boldsymbol{x}_b. \tag{13}$$

3.3.4 Color Correction (CC)

In practice, a 3×3 color correction matrix (CCM) is used in camera ISPs to restore the colors of the acquired image to match the human perception [15]. Similar to the AWB, camera vendors usually preset CCM_d and CCM_n for daytime and nighttime conversion, respectively [38]. The final transformation f_{cc} is often derived by linearly combining the presets as

$$\text{CCM}_{mix} = \omega_d \cdot \text{CCM}_d + \omega_n \cdot \text{CCM}_n. \tag{14}$$

As shown in Fig. 2c, this work relies on a neural network $E_{cc}(\cdot)$ to produce respective ω_d and ω_n. We compute ω_d as

$$\omega_d = E_{cc}(\{\hat{\boldsymbol{x}}_d,\ \hat{\boldsymbol{x}}_d^2\}), \tag{15}$$

where $\hat{\boldsymbol{x}}_d$ is computed by multiplying daytime CCM preset with every color pixel in the down-sampled $\boldsymbol{x}_b^{\downarrow}$ of size $128 \times 128 \times 3$ as $\hat{\boldsymbol{x}}_d = \text{CCM}_d \cdot \boldsymbol{x}_b^{\downarrow}$. The same procedure is applied to generate $\hat{\boldsymbol{x}}_n$, $\hat{\boldsymbol{x}}_n^2$ and compute ω_n. During the training process, both CCM_d and CCM_n are randomly initialized following the same setting defined for r_i and b_i in f_{wb}.

Then (14) is used to compute the CCM_{mix} as

$$\boldsymbol{x}_{cc} = f_{cc} \circ \boldsymbol{x}_b = \text{CCM}_{mix} \cdot \boldsymbol{x}_b. \tag{16}$$

The same $\boldsymbol{x}_{cc}$ may be produced by different $\boldsymbol{x}_b$ and different CCM scaling. Thus, following the discussions for g_{wb}, we use $E_{cc}^{-1}(\cdot)$ with color temperature prior θ to derive inverse weights ρ_d and ρ_n of g_{cc}, as $\rho_d = E_{cc}^{-1}(\{\hat{\boldsymbol{x}}_d,\ \hat{\boldsymbol{x}}_d^2,\ \theta\})$ and $\rho_n = E_{cc}^{-1}(\{\hat{\boldsymbol{x}}_n, \hat{\boldsymbol{x}}_n^2,\ \theta\})$. Thereafter we can easily obtain CCM_{mix}^{-1} as

$$\text{CCM}_{mix}^{-1} = (\rho_d \cdot \text{CCM}_d + \rho_n \cdot \text{CCM}_n)^{-1}. \tag{17}$$

Finally, we have

$$\boldsymbol{x}_b = g_{cc} \circ \boldsymbol{x}_{cc} = \text{CCM}_{mix}^{-1} \cdot \boldsymbol{x}_{cc}. \tag{18}$$

3.3.5 Gamma Correction

Gamma correction is used to match the non-linear characteristics of a display device or human perception [39]. We adopt the correction function recommended in ITU-R BT. 709 standard [40], noted as f_g, which is widely used in commodity ISPs today [41]. Additional details are provided in the supplementary material.

3.4 Training Loss

We use three loss functions, denoted as $\mathcal{L}_{adv}$, $\mathcal{L}_{cycle}$ and $\mathcal{L}_{var}$, to train the Unpaired CycleR2R. The overall loss used to train our Unpaired CycleR2R can be written as

$$\mathcal{L} = \mathcal{L}_{adv} + \mathcal{L}_{cycle} + \mathcal{L}_{var}. \tag{19}$$

First, a discriminator D_{RAW} is applied to measure the similarity between generated and real images. The discriminator can be further decomposed as D_{color} and D_{bright}, where D_{color} discriminates color discrepancy using 2D log-chroma histogram [42] and D_{bright} discriminates brightness discrepancy using 1D grayscale histogram. D_{color} stacks five convolutional layers with Leaky ReLU [43] and D_{bright} uses five linear layers. The outputs of D_{color} and D_{bright} are added together as the output of D_{RAW}. We update the parameters of g_{invISP} and D_{RAW} by minimizing the adversarial loss $\mathcal{L}_{adv}$ given as

$$\mathcal{L}_{adv}^{G} = \|1 - D_{\text{RAW}}(g_{\text{invISP}}(\boldsymbol{y}))\|_2, \tag{20}$$

$$\mathcal{L}_{adv}^{D} = \|1 - D_{\text{RAW}}(\boldsymbol{x})\|_2 + \|D_{\text{RAW}}(g_{\text{invISP}}(\boldsymbol{y}))\|_2, \tag{21}$$

$$\mathcal{L}_{adv} = \mathcal{L}_{adv}^{G} + \mathcal{L}_{adv}^{D}. \tag{22}$$

A cycle-consistency loss $\mathcal{L}_{cycle}$ is used to indirectly optimize θ and ϕ considering the assumption that RAW images captured under all possible illumination settings of the scene shall be converted into the same RGB sample. Thus the reconstructed RGB from the simRAW, given as $\overline{\boldsymbol{y}} = f_{\text{ISP}} \circ g_{\text{invISP}} \circ \boldsymbol{y}$, should be as close to the original RGB as possible, which gives us the following loss:

$$\mathcal{L}_{cycle} = \|\overline{\boldsymbol{y}} - \boldsymbol{y}\|_1. \tag{23}$$

The cycle-consistency constraint often leads to the one-to-one mapping of g_{invISP} in optimization [44]. To assure the one-to-many mapping of g_{invISP} in practice, another variant loss $\mathcal{L}_{var}$ is used with which we wish to enlarge the distance between two simRAW images $\boldsymbol{x}_1$ and $\boldsymbol{x}_2$ under two different illumination settings: $(\theta_1,\ \phi_1)$ and $(\theta_2,\ \phi_2)$. To independently evaluate the distance of color and brightness attributes, we measure the loss $\mathcal{L}_{var}$ in YUV space ($\boldsymbol{x}_1 \rightarrow \{\text{y}_1,\ \text{u}_1,\ \text{v}_1\}$, $\boldsymbol{x}_2 \rightarrow \{\text{y}_2,\ \text{u}_2,\ \text{v}_2\}$) as

$$\mathcal{L}_{var} = -\frac{\|\{\text{u}_1, \text{v}_1\} - \{\text{u}_2, \text{v}_2\}\|_2}{\|\theta_1 - \theta_2\|_2} - \frac{\|\text{y}_1 - \text{y}_2\|_2}{\|\phi_1 - \phi_2\|_2}. \tag{24}$$

4 RAW-domain Task Execution

The generated simRAW images can be used to train RAW-domain models for various tasks. We discuss high-level object detection and low-level image compression tasks, for which we refine well-known models originally developed for RGB images.

4.1 High-Level Object Detection

Object detectors [12], [46]–[49] have achieved great success in detecting objects in RGB images. The performance of off-the-shelf RGB-domain models such as YOLOv3[3] Fig. 3a presents an example where object is not detected on RAW image. The "Naive Baseline" in Table 2, 5 also show a sharp loss in performance. This is counter-intuitive because sensor RAW data with a larger dynamic range shall contain more information on the physical scene than its ISP-processed RGB sample.

We argue that the vastly diverse distribution of RAW images significantly undermines the representation capacity of DNNs originally trained using RGB samples. We first use analytical approximation to show the impact of RAW data distribution on both convolution (Conv) and batch normalization (BN) layers commonly adopted in learned detectors [12], [50]; and then apply the gamma correction to regularize RAW image distribution for RAW-domain task inference.

3. We use YOLOv3 because it is vastly used in products; but our method can be easily extended to other object detectors.

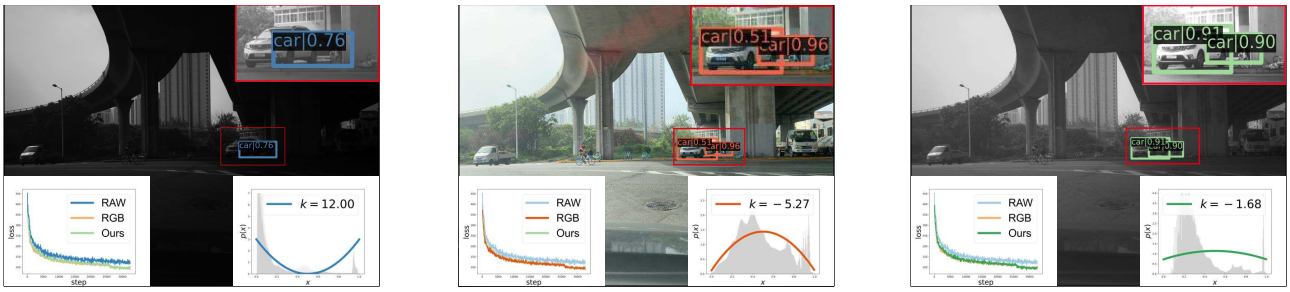

(a) The impact on Conv layer.

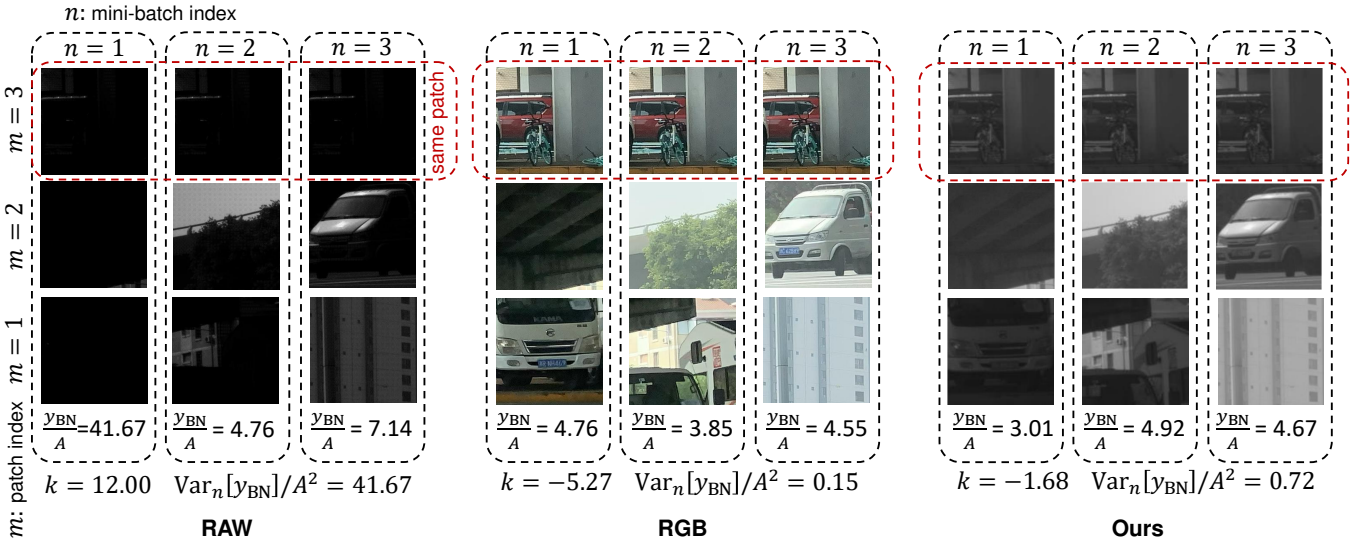

(b) The impact on BN layer.

Fig. 3: **Distribution impact of samples in native RAW, RGB, and Gamma-corrected (Ours) spaces.** YOLOv3 is refined specifically for each domain space to quantify the distribution impact. (a) The fitted histogram distribution using (25) is shown in the lower right corner, where the RAW image has the largest value of k. As can be seen from the training loss plotted in the lower left corner, the convergence speed of the RAW image is the slowest, leading to the missing of critical objects during detection; (b) The variance of features across mini-batches with the same input patch is negatively correlated to the convergence of a neural network [45]. For the investigation of feature variance after a BN layer, $\text{Var}_n[\boldsymbol{y}_{\text{BN}}]$, patches with index m from mini-batches with index n are randomly sampled in each domain. As seen, a large k also leads to imbalanced variance across mini-batches, causing an unstable training process. The $\boldsymbol{y}_{\text{BN}}$ is calculated using (31)

4.1.1 *Distribution Analysis of RAW Images*

Distribution approximation using patches. In practice, an input image $\boldsymbol{x}$ is often divided into non-overlapping small patches $\mathcal{P} = \{\boldsymbol{P}_1, \boldsymbol{P}_2, \ldots\}$ to train desired models for task inference [12], [51]. For a patch $\boldsymbol{P} \in \mathcal{P}$, its histogram can be approximated using a Gaussian distribution $\mathcal{N}(\mu,\ \sigma^2)$. To simplify modeling the distribution of pixel intensity $p(\mathbf{x})$ over the entire image using patches, we treat each patch $\boldsymbol{P}$ as a superpixel with intensity μ and assume that the $p(\mathbf{x})$ can be approximated by $p(\mu)$.

Referring to the RAW snapshot depicted in the leftmost subplot of Fig. 3a, most pixel patches are clustered in dark and bright regions, which yield histogram peaks near 0 and 1[4]. Therefore, $p(\mu)$ can be possibly hypothesized using a U-shaped function. In the meantime, without losing generality for image with proper exposure control, the mean of the entire image shall be close to the middle level of the dynamic range, which, in other words, for normalized RAW image, $\mathbb{E}[p(\mu)] = 0.5$. It then leads us to approximate $p(\mu)$ using a quadratic function:

$$p(\mathbf{x}) \approx p(\mu) \approx k\mu^2 - k\mu + \frac{k}{6} + 1, \tag{25}$$

with $0 < k \leq 12$ to guarantee $\min\{p(\mu)\} \geq 0$. Coincidentally, (25) also models the histogram of normalized RGB image very well but has the $k < 0$. As seen, k can be used to characterize the distribution of the input image (RAW or RGB). We next show that k impacts the performance of Conv and BN layers analytically, which in turn, explains why native YOLOv3 trained for RGB images cannot be directly used to process RAW samples.

Effect of k on convergence. Suppose $\boldsymbol{w} \in \mathbb{R}^{S\times S}$ denotes the Conv kernel weights randomly initialized with $\mathcal{U}(-\eta,\ \eta),\ \eta \to 0$, and $\mathbf{b}$ is the Conv bias that is randomly

4. Sensor RAW images are normalized to the range of [0,1] for processing.

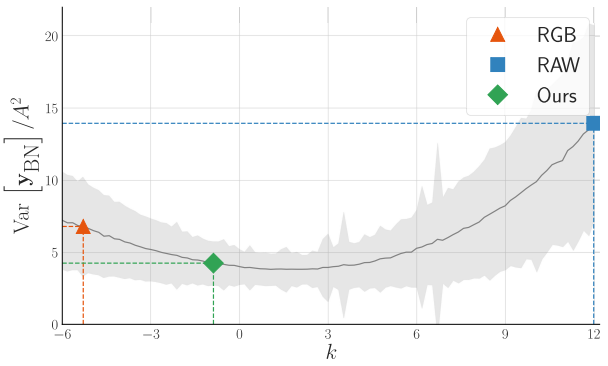

Fig. 4: $\text{Var}_n[\boldsymbol{y}_{\texttt{BN}}]/A^2$ **vs.** k.

initialized in same manner as the weights. Then a single layer of CNN can be represented as

$$\boldsymbol{y} = \boldsymbol{w} * \tilde{\boldsymbol{x}} + \mathbf{b}, \tag{26}$$

where $\tilde{\boldsymbol{x}} = \boldsymbol{x} - 0.5$ shifts the center to zero. As for the bounding box regression of the input patch $\boldsymbol{P} \sim \mathcal{N}(\mu, \sigma^2)$ in YOLOv3 [12], the loss function $\mathcal{L}$ is

$$\mathcal{L} = \frac{1}{H \times W}(\boldsymbol{w} * (\boldsymbol{P} - 0.5) + \mathbf{b} - \hat{\mathbf{y}})^2, \tag{27}$$

having $\hat{\mathbf{y}}$ as the ground truth label, and H/W as the height/width of $\boldsymbol{P}$.

For each training iteration, the weight $w \in \boldsymbol{w}$ is updated with learning rate α, i.e., $w \leftarrow w - \alpha\frac{\partial \mathcal{L}}{\partial w}$. The stability of parameter update is directly related to the variance of the gradient $\text{Var}[\frac{\partial \mathcal{L}}{\partial w}]$ as shown in [50]. This variance is approximately given as

$$\text{Var}[\frac{\partial \mathcal{L}}{\partial w}] \approx C^2\text{Var}[\tilde{\mu}^2] + D^2\text{Var}[\tilde{\mu}] + \text{const}, \tag{28}$$

where $\tilde{\mu} = \mu - 0.5$, $C = 2\sum w = 2S^2\mathbb{E}[w]$, and D is a constant. Since w is randomly initialized with a small value close to zero, $\mathbb{E}[w] \approx 0$, which simplifies (28) to:

$$\text{Var}[\frac{\partial \mathcal{L}}{\partial w}] \approx D^2\text{Var}[\tilde{\mu}] + \text{const} = \frac{D^2}{180}k + \text{const}. \tag{29}$$

This shows that the variance of the gradient is directly related to the parameter k. A larger k provides larger $\text{Var}[\frac{\partial \mathcal{L}}{\partial w}]$, making the convergence of the Conv weights more difficult and the CNN model unreliable. The proofs of (28) and (29) are provided in the Supplemental Material.

Effect of k on batch normalization. Batch Normalization [52] (BN) randomly splits a batch of training samples into mini-batches during training iteration to assure stability. A BN layer is usually placed after a convolutional layer in order to normalize the output features. Given an input patch with index m from a mini-batch with index n of size M, the output of the BN layer is given by:

$$\boldsymbol{y}_{\texttt{BN}} = \text{BN}(\boldsymbol{y}^{\ell mn}) = \gamma\frac{\boldsymbol{y}^{\ell mn} - \mathbb{E}_m[\boldsymbol{y}^{\ell mn}]}{\sqrt{\text{Var}_m[\boldsymbol{y}^{\ell mn}]}} + \beta, \tag{30}$$

where γ and β are learnable parameters, and $\boldsymbol{y}^{\ell mn}$ is the feature of layer ℓ.

It is vital for the convergence of a neural network that the mean and variance of features with the same input patch are similar across mini-batches during training [45]. Thus, we can measure the convergence speed of a model by the cross-batch variance $\text{Var}_n[\boldsymbol{y}_{\texttt{BN}}]$. The larger $\text{Var}_n[\boldsymbol{y}_{\texttt{BN}}]$ leads to the imbalance among mini-batches and thus yields an unstable training gradient. In the following part, we will demonstrate that $\text{Var}_n[\boldsymbol{y}_{\texttt{BN}}]$ increases significantly for RAW images having larger k, which degrades the training stability of the RAW-domain detector.

We will start by modeling the relationship between the input patch $\boldsymbol{P}^{mn}$ and $\boldsymbol{y}_{\texttt{BN}}$. As proven in [53], we have that $\mathbb{E}_m[\boldsymbol{y}^{\ell mn}]$ is approximately 0 and its variance is approximately $\alpha_l \cdot \text{Var}_m[\boldsymbol{y}^{\ell-1mn}]$, where α_l is a constant when the weight of layer l is fixed. Therefore, the relationship can be recursively derived as follows:

$$\boldsymbol{y}_{\texttt{BN}} \approx \frac{A}{\sqrt{\text{Var}_m[\boldsymbol{P}^{mn} - 0.5]}} + \beta, \tag{31}$$

where $A = \gamma \cdot \boldsymbol{y}^{\ell mn} / \prod_{i=1}^{\ell}\sqrt{\alpha_i}$ is a constant when the input patch $\boldsymbol{P}^{mn}$ is fixed.

Next, we will model the variance $\text{Var}_n[\boldsymbol{y}_{\texttt{BN}}]$ across mini-batches. Given (31), we simplify the variance as:

$$\text{Var}_n[\boldsymbol{y}_{\texttt{BN}}] \approx A^2 \cdot \underset{n}{\text{Var}}[\frac{1}{\sqrt{\text{Var}_m[\boldsymbol{P}^{mn} - 0.5]}}]. \tag{32}$$

Due to the limited batch size M, it is difficult to obtain a closed-form probability distribution of $\boldsymbol{P}^{mn}$. Therefore, we resort to sampling simulations for approximation. To simplify the problem, we neglect the variance in a patch and represent it with its mean value μ. We obtain the value of $\text{Var}_n[\boldsymbol{y}_{\texttt{BN}}]/A^2$ using 5000 randomly-sampled mini-batches that contain the same patch $\boldsymbol{P}^{mn}$ characterized by $p(\mu)$ in (25). The whole process is repeated 5000 times using different randomly-sampled $\boldsymbol{P}^{mn}$ to obtain the average value of $\text{Var}_n[\boldsymbol{y}_{\texttt{BN}}]/A^2$. Figure 4 shows the quantitative approximation between $\text{Var}_n[\boldsymbol{y}_{\texttt{BN}}]/A^2$ and k. It is clear that $\text{Var}_n[\boldsymbol{y}_{\texttt{BN}}]$ increases significantly for larger values of k.

Remark. As seen, larger k induced by the RAW input slows the convergence of convolutional weights and yields unstable batch normalization, making the underlying model unreliable and inefficient, which requires us to regularize the distribution of RAW images for robust performance.

4.1.2 *Distribution Regularization Using Gamma Correction*

To eliminate the negative impact of a large k of a RAW image for RAW-domain detection, we use a simple-yet-efficient gamma correction defined in ITU-R BT.709 [40] to reduce the k by brightening the dark area and darkening the light area. As shown in the rightmost subplot of Fig. 3, those sub-images generated by the gamma correction effectively reduce the k of the original RAW input, making the convergence of RAW-domain detector faster and the resultant model more robust with better performance (see Table 5).

4.2 Low-Level RAW Image Compression

Applications often mandate the archival of images for after-action review and analysis, leading to the desire for high-efficiency image compression. Existing image codecs mainly deal with RGB, monochrome, or YCbCr color spaces. In this

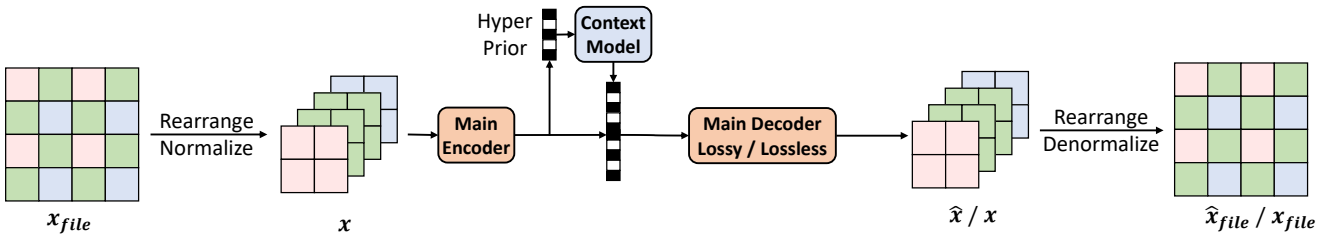

(a) RAW Image Compression (RIC) Architecture

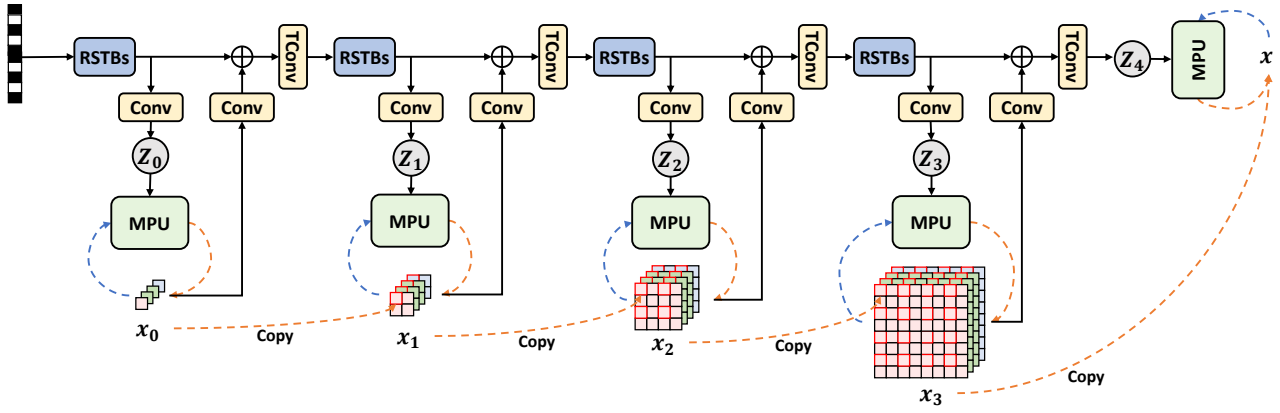

(b) Lossless RIC Decoder

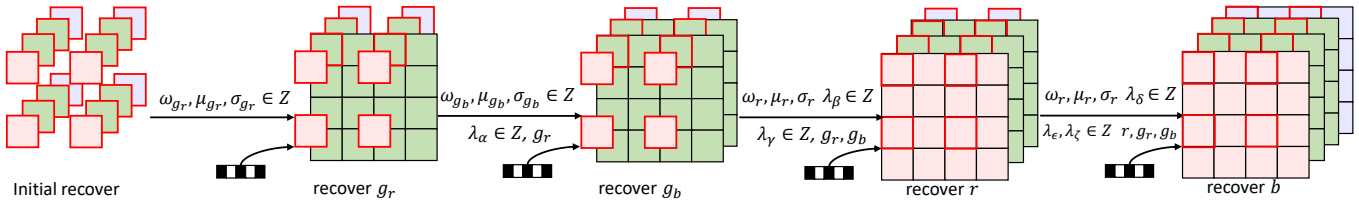

(c) Multichannel Processing Unit (MPU)

Fig. 5: **RAW Image Compression (RIC).** (a) Similar TinyLIC architectures are used for both lossy and lossless RIC. More details about the lossy pipeline are in [13]. (b) The detailed architecture of the lossless decoder. $\boldsymbol{Z}_i$, $i \in [0, 4]$ aggregates low-resolution information to characterize the logistic distribution for element probability derivation. The probability is used for both encoding (blue) and decoding (orange). In decoding, $\boldsymbol{x}$ are gradually recovered with progressive decoding; (c) Multichannel Processing Unit (MPU) is devised to process the element in $\boldsymbol{x}_i$ with the probability derived from the $\boldsymbol{Z}_i$ under a predefined order, *e.g.*, $g_r \rightarrow g_b \rightarrow r \rightarrow b$. Arithmetic decoding is omitted. Residual Swin Transformer Blocks (RSTBs) are stacked to aggregate and embed necessary information. The Conv and TConv stand for the convolutional and transposed convolutional layer respectively.

section, we explore the feasibility of encoding RAW images directly. We suggest using learned image compression for this purpose, not only because of its superior coding efficiency [13], [54], [55] but also its flexibility to support the coding of various image sources.

4.2.1 *Lossy RAW Image Compression (RIC)*

We extend the TinyLIC proposed in [13] for lossy RIC with the following amendments shown in Fig. 5a:

1) *Rearrangement:* First, we follow [56] to rearrange Bayer RAWs to RGGB presentation. At each pixel position, its spectral components, e.g., (R, G, G, B), are stacked for compression, which is similar to the pixel of (R, G, B) used in default TinyLIC;
2) *Normalization:* We normalize the original Bayer RAW files through linearization using

$$\boldsymbol{x} = \frac{\boldsymbol{x}_{file} - \texttt{blackLev}}{\texttt{saturationLev} - \texttt{blackLev}}, \tag{33}$$

where $\boldsymbol{x}_{file}$ is the Bayer RAW collected by an image sensor, and $\boldsymbol{x}$ is normalized RAW in the range of [0, 1]. `saturationLev` and `blackLev` indicate the dynamic range of image pixels, which can be directly retrieved from the EXIF metadata of the RAW input.

The `saturationLev` is related to the bit depth supported by the specific camera for RAW acquisition. It is the same for all RAW images captured by the same camera. We choose to embed the `blackLev` coefficients globally (e.g., $1 \times 16 = 16$ bits present $< 0.03\,\%$ of the total bits used by a 512×512 image) to ensure the encoder-decoder consistency. Stacking RGGB components could let the lossy RIC explicitly learn the inter-spectral or inter-color correlations. As will be shown later, our lossy RIC significantly outperforms the traditional methods on RAW encoding. For other imaging patterns, e.g., RYYB used in the Huawei P30 Pro can be processed similarly.

4.2.2 Lossless RIC

Numerous applications need to cache RAW images losslessly for future processing (e.g., professional photography, safety-critical event record, etc.). We further extend the lossy RIC to support the lossless mode.

Multiresolution Decoding. In lossy RIC, the processing steps in the main encoder-decoder pair are symmetrically mirrored [13]. In lossless RIC, we redesign the main decoder while keeping the same main encoder as in lossy RIC. Instead of decoding the full-resolution reconstruction in one shot, we gradually decode the pixels to refine the image resolution from $\boldsymbol{x}_0$ to $\boldsymbol{x}_4$ ($\boldsymbol{x}_4 = \boldsymbol{x}$) in Fig. 5b. As seen, the compression performance is improved by exploiting the correlations from previously-decoded neighbors. Such progressive decoding enables the low-resolution preview that is not available in existing approaches [57], [58] but is a highly-desired tool in commercial cameras.

The lossless decoding of $\boldsymbol{x}_i$, $i \in [1, 4]$ is organized as:

1) The $\boldsymbol{x}_i$ is dyadically upsampled from $\boldsymbol{x}_{i-1}$ with 2× scaling at each dimension, i.e., each pixel in $\boldsymbol{x}_{i-1}$ is expanded to four pixels arranged in a local 2×2 patch in $\boldsymbol{x}_i$;
2) As in Fig. 5b, the upper-left pixel of each 2×2 patch of $\boldsymbol{x}_i$ is directly filled using the corresponding pixel of $\boldsymbol{x}_{i-1}$ (highlighted with red box), while the other three pixels in each 2×2 patch of $\boldsymbol{x}_i$ is decoded using the conditional probability of logistic distribution that is characterized by the $\boldsymbol{Z}_i$;

Note that a special case is made for the processing of $\boldsymbol{x}_0$ since there are no available pixels from a lower resolution scale. As a result, $\boldsymbol{Z}_0$ is generated by parsing the compressed bitstream only.

Multichannel Processing. As seen, $\boldsymbol{Z}$[5] thoroughly aggregates information from the lower resolution scale, which is then input into the Multichannel Processing Unit (MPU) to encode/decode pixels in a predefined order to fully exploit the cross-channel correlations. Here, we use r, g_r, g_b, b to represent four Bayer pattern channels. For the MPU in Fig 5c, only $\boldsymbol{Z}$ is used to derive the probability of g_r samples for its encoding and decoding first. Then both $\boldsymbol{Z}_i$ and previously-processed samples are used to process g_b, r, and b sequentially. Here we parameterize the sample distribution P as a mixture of logistic distribution P_l [59]:

$$\begin{aligned} P(g_r \mid \boldsymbol{Z}) &= \sum_{k=1}^{K} \omega_{g_r k} \cdot P_l(g_r \mid \mu_{g_r k}, \sigma_{g_r k}) \\ P(g_b \mid \boldsymbol{Z}, g_r) &= \sum_{k=1}^{K} \omega_{g_b k} \cdot P_l(g_b \mid \tilde{\mu}_{g_b k}, \sigma_{g_b k}) \\ P(r \mid \boldsymbol{Z}, g_r, g_b) &= \sum_{k=1}^{K} \omega_{r k} \cdot P_l(r \mid \tilde{\mu}_{r k}, \sigma_{r k}) \\ P(b \mid \boldsymbol{Z}, g_r, g_b, r) &= \sum_{k=1}^{K} \omega_{b k} \cdot P_l(b \mid \tilde{\mu}_{b k}, \sigma_{b k}), \end{aligned} \tag{34}$$

where the $\tilde{\mu}$ builds the cross channels dependency:

$$\begin{aligned} \tilde{\mu}_{g_b k} &= \mu_{g_r k} + \lambda_{\alpha k} \cdot g_r, \\ \tilde{\mu}_{r k} &= \mu_{r k} + \lambda_{\beta k} \cdot g_r + \lambda_{\gamma k} \cdot g_b, \\ \tilde{\mu}_{b k} &= \mu_{b k} + \lambda_{\delta k} \cdot g_r + \lambda_{\epsilon k} \cdot g_b + \lambda_{\zeta k} \cdot r. \end{aligned} \tag{35}$$

The logistic function $P_l(x|\mu, \sigma)$ can be easily calculated using $\{\text{sigmoid}(\frac{x-\mu+1/2s}{\sigma})$ - $\text{sigmoid}(\frac{x-\mu-1/2s}{\sigma})\}$ with s = `saturationLev-blackLev`. Parameters μ, σ, ω and λ are a part of the prior $\boldsymbol{Z}$ and we set $K = 10$ as in [59], [60]. In training, we only need to minimize the entropy loss $\mathcal{L} = -\mathbb{E}\left[\log P(r, g_r, g_b, b \mid \boldsymbol{Z})\right]$ for lossless compression.

5. The subscript index i is omitted in $\boldsymbol{Z}_i$ for general assumption.

5 Experimental Results

This section presents experiments where we execute tasks using RAW images directly.

5.1 Experiment Setup

We first list the RAW and RGB image datasets used in experiments, and then discuss the setup of the proposed Unpaired CycleR2R to generate simRAW images.

5.1.1 Datasets

MultiRAW is a high-resolution RAW image dataset acquired using popular camera sensors. Specifically, the entire dataset was shot using five cameras fixed on the car dashboard at different times (day and night) and geolocations (rural, tunnel, and urban areas) to simulate real-life autonomous driving. Having RAW images from different cameras allows us to validate the generalization of the proposed method.

Table 1 provides details about 7,469 RAW images that cover a variety of application scenarios (mobile/ industrial/autopilot), imaging Bayer patterns (RGGB/RYYB), and bit depths (e.g., 10/12/16/24). All RAW images could be converted to RGB counterparts using the corresponding in-camera ISP. Fine-grained detection and segmentation bounding boxes for cars, persons, traffic lights, and traffic signs are labeled manually by a third-party professional image labeling firm.

Among the RAW images captured by iPhone XSmax, Huawei P30pro, asi 294mcpro, and the LUCID TRI054S, we randomly selected 30 % samples as the test set and the remaining ones as the training set. For RAW images acquired by Oneplus 5t, we use all of them for testing.

BDD100K [29] is one of the largest autonomous driving datasets. It contains 100 k RGB images taken in diverse scenes such as city streets, residential areas, and highways, making object detection more challenging and close to real-life scenarios. We follow the official data splitting of 70 k, 10 k, and 20 k images for training, validation, and testing, respectively. To avoid the discrepancy of traffic signs captured in *BDD100K* (*e.g.*, collected across tens of different countries) and MultiRAW (*e.g.*, collected mainly in mainland China) datasets, we only conducted training and testing on the "car" category that has the largest number of objects (*e.g.*, >55 %) and presents the smallest differences.

Flicker2W [63] is widely used to train learned image compressors [13]. Although we collected more than 7k samples in MultiRAW, its size is less than that of RGB image datasets (*e.g.*, 100k in *BDD100K*) used in popular tasks. To train robust models, we apply our Unpaired CycleR2R to generate simRAW images using popular RGB datasets. For example, all RGB samples in *BDD100K* and *Flickr2W* are converted to RAW images to retrain existing RGB-domain models.

TABLE 1: **MultiRAW Dataset:** A collection of 7,469 labeled RAW images from five diverse camera sensors. The dataset covers various settings (e.g., Bayer pattern, bit depth) and application scenarios.

Camera	Usage	Bayer Pattern	Bit Depth	Task	Scenarios	No. of Images
iPhone XSmax	Mobile	RGGB	12	Detection, Segmentation	Day	1153
Huawei P30pro	Mobile	RYYB	12	Detection	Day, Night	3004
asi 294mcpro	Industrial	RGGB	14	Detection	Day, Night	2950
Oneplus 5t	Mobile	RGGB	10	Detection	Day	101
LUCID TRI054S	Autopilot	RGGB	24	Detection	Day, Tunnel	261

TABLE 2: **Recall and Average Precision (AP) of Object Detection on the testing set of iPhone RAWs.** RGB detector is trained using original RGB images in *BDD100K* [29] (e.g., RGB_b); Various simRAW datasets associated with RGB_b are generated using different methods which are simply marked as simRAW_b to train the RAW detector. The testing RAW images in iPhone RAW RAW_i and their paired RGB images in RGB_i converted using built-in iPhone ISP are tested accordingly. All detectors are shared with the same head, *i.e.*, YOLOv3 [12] and the same backbone, *i.e.*, MobileNetV2 [61] for a fair comparison. ♠ Baselines, ♦ Domain Adaptation Solutions, ■ invISP Methods, ★ Ours.

Method	invISP Training	Detector Training	Detector Testing	Recall	AP
♠ Naive Baseline	-	RGB_b	RAW_i	67.5	51.1
♠ RGB Baseline	-	RGB_b	RGB_i	74.7	55.6
♦ DA-Faster (CVPR'18) [62]	-	RGB_b, RAW_i	RAW_i	13.7	12.9
♦ MS-DAYOLO (ICIP'21) [18]	-	RGB_b, RAW_i	RAW_i	31.2	29.7
♦ AT (CVPR'22) [19]	-	RGB_b, RAW_i	RAW_i	68.9	53.2
■ InvGamma (ICIP'19) [25]	RGB_i, RAW_i	simRAW_b	RAW_i	68.6	48.7
■ CycleISP (CVPR'20) [14]	RGB_i, RAW_i	simRAW_b	RAW_i	71.6	52.7
■ CIE-XYZ Net (TPAMI'21) [15]	RGB_i, RAW_i	simRAW_b	RAW_i	72.2	53.0
■ MBISPLD (AAAI'22) [16]	RGB_i, RAW_i	simRAW_b	RAW_i	73.0	53.7
★ **Unpaired CycleR2R**	RGB_b, RAW_i	simRAW_b	RAW_i	**76.1**	**59.1**

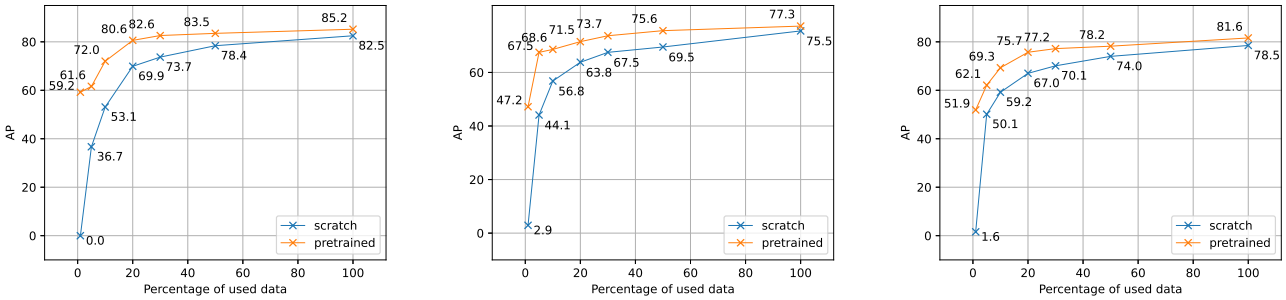

(a) iPhone XSmax. (b) Huawei P30pro. (c) asi 294mcpro.

Fig. 6: **Few-shot model finetuning using limited camera RAWs.** The "pretrained" YOLOv3 is pretrained using samples in simRAW_b generated by our invISP, and the "scratch" model is first randomly initialized and then directly trained using labeled real RAW images from a specific camera model.

5.1.2 *Training Unpaired CycleR2R for simRAW Generation*

We first train our Unpaired CycleR2R to generate simRAW images to finetune/retrain existing RGB-domain models for RAW-domain tasks. For example, unpaired RGB and iPhone RAW images that were respectively chosen from the *BDD100K* [29] (without knowledge of camera sensors) and MultiRAW datasets are used to train the Unpaired CycleR2R for the high-level detector. We also use the original *Flicker2W* [63] along with the random iPhone RAW images to train the Unpaired CycleR2R for the low-level compressor.

We train the model using randomly selected patches of size 512×512 and batch size 8. We applied random scaling and reflection to augment the training data. A single NVIDIA 3090Ti was used for $20,000$ iterations of an Adam optimizer with a learning rate $5 \cdot 10^{-4}$. The discriminators were set with a learning rate at $5 \cdot 10^{-5}$. The momentum for Adam is set to $\{0.9, 0.99\}$. Finally, g_{invISP} from the Unpaired CycleR2R framework was used to produce simRAW_b and simRAW_f images using RGB images in *BDD100K* [29] and *Flicker2W* [63].

TABLE 3: **The lossless compression results on MultiRAW.**

Method	Camera	Latency (s)		BPP
		Encoder	Decoder	
CinemaDNG	iPhone XSmax (RGGB/12 bits) 4032 × 3024	0.49	0.52	9.51
JPEG XL		19.73	6.38	5.46
FLIF		38.67	8.76	5.46
PNG		0.44	0.24	7.98
Lossless RIC-1 %		1.35	0.78	5.29
Lossless RIC-100 %				**5.21**
CinemaDNG	Huawei P30pro (RYYB/12 bits) 4032 × 3024	0.42	0.46	9.52
JPEG XL		21.37	6.67	5.62
FLIF		41.67	9.56	5.60
PNG		0.39	0.22	7.93
Lossless RIC-1 %		1.32	0.79	5.16
Lossless RIC-100 %				**5.12**
CinemaDNG	asi 294mcpro (RGGB/14 bits) 4144 × 2822	0.40	0.44	18.85
JPEG XL		9.37	2.91	1.46
FLIF		18.83	4.26	1.36
PNG		0.32	0.17	2.86
Lossless RIC-1 %		1.83	0.81	0.77
Lossless RIC-100 %				**0.75**

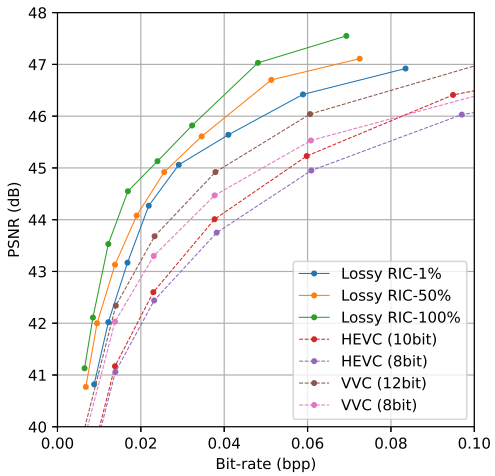

Fig. 7: **Rate-distortion Performance of Lossy RIC.** These testing RAW images are from our MultiRAW dataset and distortion is measured in the RAW domain. All RICs are pre-trained with simRAW images and fine-tuned using a limited number of real captured RAWs. Lossy RIC-1 %, Lossy RIC-50 % and Lossy RIC-100 % denote 1 %, 50 % and 100 % real RAW samples are used for fine-tuning. HEVC and VVC Intra coders are evaluated for comparison.

5.2 RAW-domain Object Detection

This section shows that the object detector trained on simRAW images can directly process real-life RAW images and provide good accuracy. Then, we discuss how the performance of a simRAW-pretrained detector can be further improved by the few-shot finetuning using a limited number of labeled real RAW images from a camera used in a specific application scenario. Our results show that such a few-shot fine-tuned detector consistently outperforms the model trained from scratch using the same set of real RAW images.

Training RAW-domain detector. We chose the popular YOLOv3 as our baseline object detector [12] and the prevalent MobileNetv2 [61] as the backbone.

- RAW-domain YOLOv3 can be trained using simRAW_b set generated from the RGB samples (RGB_b) in *BDD100K* using various invISP methods [14]–[16], [25] (see Table 2). We trained YOLOv3 using SGD with the batch size at 8, a momentum of 0.9, and a weight decay of 10^{-4}. A learning rate of 0.02 was used in training for 30 epochs.
- RAW-domain YOLOv3 can also be retrained using unpaired RGB_b and RAW_i sets of respective *BDD100K* and iPhone RAW (a subset of MultiRAW) through the use of domain adaptation (DA) techniques following their official settings [18], [19], [62].

We tested the trained models on the test set of RAW_i.

Remark. For the invISP methods listed in Table 2 that strictly required RGB-RAW pairs from a specific camera model, we fine-tuned their pre-trained models using our MultiRAW dataset by applying the same training settings used to train our Unpaired Cycle R2R model (*i.e.* epochs, training patches).

Comparative Studies. Table 2 reports the object detection accuracy in the RAW domain. In general, our model achieves SOTA performance with a large margin (more than 5.4 %). DA approaches in [18], [62] failed to learn the effective mapping between RAW and RGB samples. This is mainly because the domain difference between RAW and RGB samples is fundamentally different from that between two RGB sets studied in [18], [62]. A self-supervised learning approach was proposed [19] by introducing more generic representation features, which then boosted the performance noticeably. However, the sizeable training resources (96 G GPU memory for five days) limit its adoption in practical applications. And as we mentioned above, previous invISP methods [14]–[16], [25] modeled a known camera could not convert the RGB from an unknown camera properly. More importantly, our model is the only one exceeding the RGB baseline that is widely deployed in practical applications. These results offer promising prospects for RAW-domain task inference, for which existing RGB-domain models are retrained using samples in simRAW_b that are generated using the Unpaired CycleR2R. In contrast, directly feeding RAW images to the RGB-domain detector presents inferior performance as exemplified in the Naive Baseline that lacks any RAW-domain knowledge.

The performance of simRAW-pretrained YOLOv3 can be further improved by few-shot learning using a limited number of labeled real RAW images from a specific camera model. As shown in Fig. 6, the detection accuracy is improved consistently for three cameras. We also provide the model accuracy when training YOLOv3 from scratch, for which the model is first randomly initialized and then trained using the same labeled real RAWs. The results show that fine-tuning simRAW-pretrained YOLOv3 consistently outperforms training the model from scratch. More specifically, 2.7 % - 59.2 % AP improvement for iPhone XSmax, 1.8 % - 44.3 % for Huawei P30pro, and 3.1 % - 50.4 % for

asi 294mcpro clearly reveals the advantages of pretraining a model using simRAW images.

Implementation convenience. Given that our method does not require paired RAW and RGB samples to train the invISP for the generation of simRAW images, it is much easier for practitioners to use our method to promote RAW-domain tasks. Furthermore, generated simRAW images can also be used to train/finetune models for other tasks, such as the segmentation method discussed in the supplementary material.

Note that most of the domain adaptation approaches [18], [62] need to modify the underlying model for each individual task manually. For example, Chen et al. [62] changed the predictor head of bounding box (bbox) and Li et al. [19] added bbox relevant loss functions which makes the migration to other tasks without bbox prediction impractical. In contrast, our method just retrains existing RGB-domain models (deployed in practice) to process RAW inputs. This makes our method suitable for various tasks, including detection and segmentation. Please see the supplementary material for more details.

TABLE 4: **Ablation of modular components of Unpaired CycleR2R**. KL divergence was assessed between real and simulated RAW images. Additionally, Recall and Average Precision (AP) metrics were evaluated using various RAW-domain detectors. These detectors were trained on simRAW images, generated by adapting modular settings in Unpaired CycleR2R, including Auto White Balance (AWB), Brightness Adjustment (BA) and Color Correction (CC), Illumination Estimation Module (IEM) and variance loss $\mathcal{L}_{var}$.

Method	AWB	BA	CC	IEM+$\mathcal{L}_{var}$	KL	Recall	AP
InvGamma [25]	-	-	-	-	0.25	68.6	47.7
CycleISP [14]	-	-	-	-	0.08	71.6	52.7
CIE-XYZ Net [15]	-	-	-	-	0.13	72.2	53.0
MBISPLD [16]	-	-	-	-	0.11	73.0	53.7
Unpaired CycleR2R	✓				0.12	71.9	53.6
	✓	✓			0.10	72.5	54.9
	✓	✓	✓		0.09	74.9	56.1
	✓	✓	✓	✓	**0.06**	**76.1**	**59.1**

5.3 RAW Image Compression (RIC)

This section presents results for RAW Image Compression (RIC) as a typical low-level task. Similar to Sec. 5.2, we first demonstrate the feasibility and performance of simRAW-pretrained RIC, and then illustrate further improvement by few-shot finetuning using real RAW images.

Training RAW-domain RIC. We use unpaired RGB and RAW samples from Flicker2W and iPhone RAW datasets to train the Unpaired Cycle R2R and generate simRAW images. Given that we do not need to label the semantic cues for high-level tasks, we use less than $1\,\%$ (*i.e.*, 10) real and random RAW images to train our model. We present this challenging setting to demonstrate that our method can be fine-tuned using a small number of real images, which can be especially useful in real-world settings with limited training data.

Then we follow the same procedure in Sec. 5.1 to convert native RGB images in *Flicker2W* [63] to simRAW images (*i.e.* simRAW$_f$) for the training of lossy and lossless RIC models, marked as Lossy RIC-1 $\%$ and Lossless RIC-1 $\%$. We also fine-tune these simRAW-pretrained models with more real RAW data for further improvement (see Lossy and Lossless RIC-100 $\%$).

All RIC training threads run on a single NVIDIA 3090Ti GPU for a total of 400 epochs. Adam optimizer with the learning rate of 10^{-4} and batch size of 8 for each iteration. For lossy RIC, eight models are trained to provide 8 different bit rates (or quality levels). A pre-trained high-rate model is used to initialize the weights and to train a model for the lossless mode.

Comparative studies of Lossy RIC. We compare our Lossy RIC with HEVC Intra and VVC Intra through the compression of MultiRAW test set. Because traditional video codecs cannot handle the RAW images directly, we decompose the spectral channels (RG$_r$G$_b$B) of a RAW image into an RGB image *i.e.*, RG_rB and a residual image r$_g$ = G$_b$ - G$_r$ following the Apple ProRes RAW setting, which then can be encoded by HEVC Intra, VVC Intra, respectively. Here, we apply the reference software models of HEVC and VVC for intra-compression (i.e., HEVC 16.22[6] and VTM 11.0[7]). Note that we perform the linearization on the RAW image by scaling the pixels in [0, 1] range. We then scale them to different bit depths before feeding them into the HEVC or VVC Intra coder. Since both HEVC and VVC can support higher bit depth beyond 8-bit precision, we have also tried out the 10-bit and 12-bit precision. As such, we can alleviate the quantization loss as much as possible. All other parameters in HEVC and VVC intra-encoders are kept same as default.

Figure 7 shows the rate-distortion performance of RAW image compression. As seen, even simRAW-pretrained lossy RIC (i.e., Lossy RIC-1 $\%$) largely outperforms state-of-the-art 12-bit VVC. When we use more real RAW images to fine-tune the pretrained lossy RIC, the compression efficiency is further improved as reported for Lossy RIC-50 $\%$ and Lossy RIC-100 $\%$ that provide 2–3 dB PSNR gains over 8 bits HEVC Intra, 1–2 dB gains over 12 bits VVC Intra across a wide bit rate range.

Figure 8 presents the reconstructions and closeups generated by the HEVC Intra, VVC Intra, and our Lossy RIC-100 $\%$. As seen, our method noticeably improves the subjective quality with sharper textures and lesser noise.

Comparative studies of Lossless RIC. Table 3 shows a comparison of our approach and other lossless codecs for the test samples in MultiRAW set, in terms of the bits per pixel (BPP). For PNG, JPEG XL, and FLIF designed for RGB images, we use the same evaluation strategy by splitting it into two images for compression. First, our Lossless RIC-1 $\%$ trained on simRAW$_f$ only already outperforms PNG (a widely-used RGB compressor) with 35–74 $\%$ reduction in BPP and CinemaDNG (a professional RAW compressor) with 45–96 $\%$ reduction in BPP, for three different cameras. Compared with JPEG XL and FLIF, our method offers up to

6. https://vcgit.hhi.fraunhofer.de/jct-vc/HM
7. https://vcgit.hhi.fraunhofer.de/jvet/VVCSoftware_VTM

12 bpp - Ground Truth	0.015 bpp 44.15 dB HEVC-8bits	0.015 bpp 44.28 dB HEVC-10bits	0.016 bpp 44.79 dB VVC-8bits	0.017 bpp 45.14 dB VVC-12bits	0.015 bpp 46.35 dB **Ours**

Fig. 8: **Qualitative Visualization.** Reconstructions and close-ups of the HEVC, VVC, and our method. Corresponding bpp and PSNR are marked. Gamma correction and brightness adjustment have been applied for a better view. *Zoom for better details.*

48 % reduction in BPP, but our method runs much faster for both encoding and decoding. Furthermore, the small gap of ($< 2\,\%$) between Lossless RIC-100 % and Lossless RIC-1 % reveals that our Unpaired CycleR2R is capable of characterizing and embedding sufficient RAW-domain knowledge using a very small amount of real RAW images. Furthermore, the simRAW images produced by our invISP are able to train a generic lossless RAW image compressor. This makes our solution very attractive for practical situations with limited real training data.

6 Ablation Studies

In this section, we first provide additional discussion on the modular components of invISP. Then we study the impact of gamma correction and illumination on RAW-domain detection. Finally, we presents the progressive decoding ability of our lossless RIC and ρ-Vision's hardware implementation.

6.1 Modular Components of Unpaired CycleR2R

Table 4 employs the Kullback-Leibler (KL) divergence alongside Recall and Average Precision (AP) to evaluate the impact of modular components within the Unpaired CycleR2R framework. The KL divergence assesses the distribution similarity between the color channels of simulated (simRAW) and real captured RAW images, with lower values indicating higher resemblance. This statistical measure is crucial for determining the realism of simRAW images utilized for training vision models. In addition to the KL divergence, Recall, and AP metrics are calculated by executing the task upon the same real RAW dataset. Here, various detectors are trained on simRAW images by activating or deactivating certain modules of our model. These metrics demonstrate that each module significantly influences task accuracy. The Illumination Estimation Module (IEM), in particular, markedly increases the AP from 56.1 % to 59.1 %. This improvement is credited to IEM's advanced simulation of diverse lighting conditions, which is more representative of real-world scenarios than traditional methods that often rely on fixed illumination settings for ISP/invISP modeling. We give some visualization samples in the Supplementary, showcasing the module's contribution to producing training data that closely mirrors genuine imaging conditions.

TABLE 5: **Impact of Gamma Correction (GC) on object detection for different cameras and different object classes.**

Domain	Camera	Vehicle	Person	Tr. Sign	Tr. Light	mAP
RGB		82.6	34.9	72.7	54.0	**61.1**
RAW w/o GC	i-12	79.2	25.3	70.2	48.6	55.8
RAW w/ GC		81.1	33.5	73.8	55.0	60.8
RGB		75.3	38.4	62.2	49.5	56.4
RAW w/o GC	HW-12	74.3	33.7	61.4	49.4	54.7
RAW w/ GC		75.5	39.4	62.0	50.9	**57.0**
RGB		76.2	34.0	66.4	60.7	58.3
RAW w/o GC	asi-14	60.2	18.5	49.7	46.8	43.8
RAW w/ GC		79.0	42.2	71.8	63.8	**64.2**

i-12 ← iPhone XSmax (12 bits); HW-12 ← Huawei P30pro (12 bits); asi-14 ← asi 294mcpro (14 bits).
Tr. Sign ← Traffic Sign; **Tr. Light** ← Traffic Light.

6.2 Gamma Correction

We prove analytically in Sec. 4.1.2 that directly feeding linear RAW images into the detector typically leads to inferior detection performance. We then suggest the gamma correction approach adjusts the input distribution and subsequently boosts the performance of RAW-domain detection. Here we offer a quantitative evaluation of the gamma correction.

For a fair comparison, we train three detectors sharing the same head (YOLOv3 [12]) and backbone (MobileNetV2 [61]) using the training samples in the proposed MultiRAW dataset. Specifically, we train an RGB-domain detector (i.e., RGB in Table 5) using the RGB images that are converted from the RAW samples with in-camera ISP, and use it to test RGB images as well. We also train two RAW-domain detectors where one option, RAW w/ GC in Table 5, applies the gamma correction to adjust training RAW samples prior to the training, and the other one, RAW w/o GC in Table 5, keeps using the same RAW samples without change.

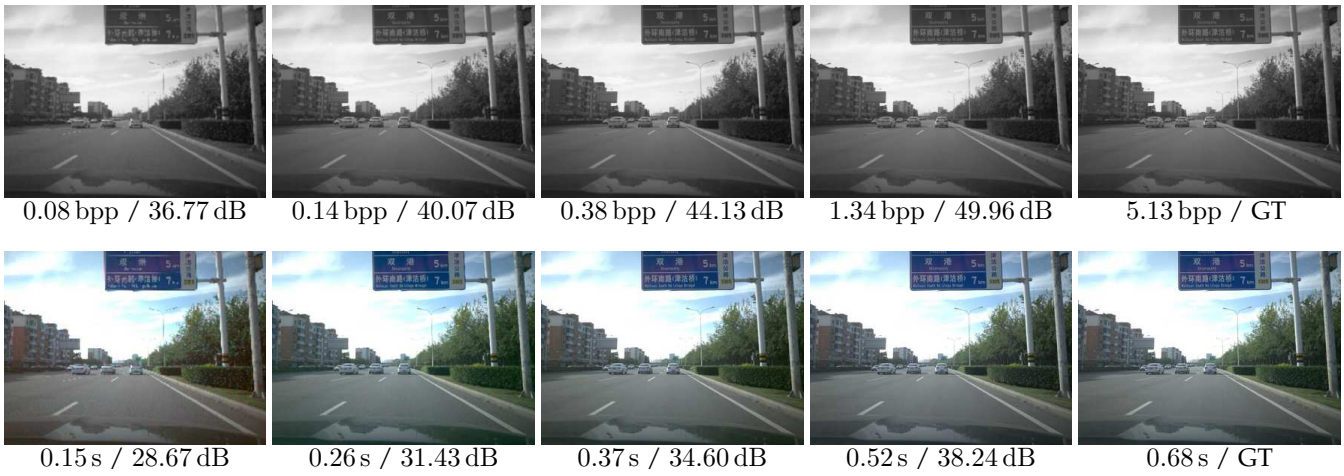

Fig. 9: **Progressive Decoding.** The gradual reconstruction of RAW images and their corresponding RGB images converted by an in-camera ISP. Bits per pixel (bpp) / PSNR (dB) is shown under RAW images. Decoding latency (s) / PSNR (dB) is also listed below RGB images. PSNR is derived against the GT (ground truth). Gamma correction and brightness adjustment have been applied for a better view. *Zoom for more details.*

TABLE 6: **Comparative analysis of object detection performance under different illumination conditions across various object sizes.**

Scenarios	Domain	mAP_{small}	mAP_{medium}	mAP_{large}	mAP
Day	RGB	19.1	54.9	73.6	58.5
	RAW	**21.2**	**57.8**	**74.7**	**60.5**
Night	RGB	17.0	49.1	63.1	56.1
	RAW	**28.2**	**54.5**	**67.7**	**59.8**

As seen, without gamma correction, the performance of the RAW-domain detector is inferior to that of the RGB-domain detector with a noticeable gap. The gamma correction significantly improves the detection results even exceeding the RGB-domain model, further confirming the analytical proof in Sec. 4.1.2. The performance improvement is larger for asi 294mcpro camera sensor that has a 14-bit dynamic range, suggesting that fine-grained spatial details in shadow and highlight parts can be well retained in high-bit-precision RAW samples for better object detection.

6.3 Illumination Influence on Detection Accuracy

The influence of illumination conditions on object detection accuracy was systematically evaluated across various object scales. The performance metrics, detailed in Table 6, reveal notable improvements when using RAW data for detection, especially under complex nighttime conditions (+3.7). This improvement is particularly pronounced for small objects (+11.2), where the RAW format's extended dynamic range facilitates the discernment of details often lost in standard 8-bit RGB images due to brightness clipping or overexposure.

Figure 10 further visualizes the detection results under various challenging illumination scenarios, such as direct sunlight, night lens flare, and complex lighting with multiple sources. As seen, RAW-domain processing can better preserve details in both bright and shadow areas which are typically overlooked in standard 8-bit RGB images due to brightness clipping or overexposure.

6.4 Progressive Decoding

Our lossless RIC model supports progressive decoding to refine the image resolution gradually, which enables the low-resolution preview of high-resolution RAW and RGB images (converted by the in-camera ISP). Such a prompt low-resolution preview (see the visualization in Fig. 9) is a useful add-on function for applications like professional photography. As also shown in Fig. 9, we can observe the restoration of high-frequency details gradually. Another useful takeaway of such progressive decoding is its inherent network transmission friendliness, with which we can still decode partial bitstream received at the client for display or consumption [64].

6.5 Hardware Implementation

We deployed our ρ-Vision framework on the Axera-Tech AX620A SoC, which facilitated a direct comparison between RAW-domain visual computing and conventional ISP processing methods. Utilizing YOLOv8-S and the MultiRAW dataset as our benchmark, the experimental outcomes underscore the superiority of ρ-Vision. Specifically, we observed a 3% increase in detection accuracy, coupled with substantial reductions in latency (72%), power consumption (62%), and memory usage (36%). Notably, these enhancements were achieved without necessitating complex modifications to the network model architecture. The benefits of our approach become even more evident under challenging conditions, such as in low-light and high dynamic range scenarios. Detailed results and further analyses can be found in our supplementary materials.

7 Conclusion

In this paper, we demonstrate that performing high-level vision tasks and low-level image compression on the camera RAW images is practically feasible and efficient. In

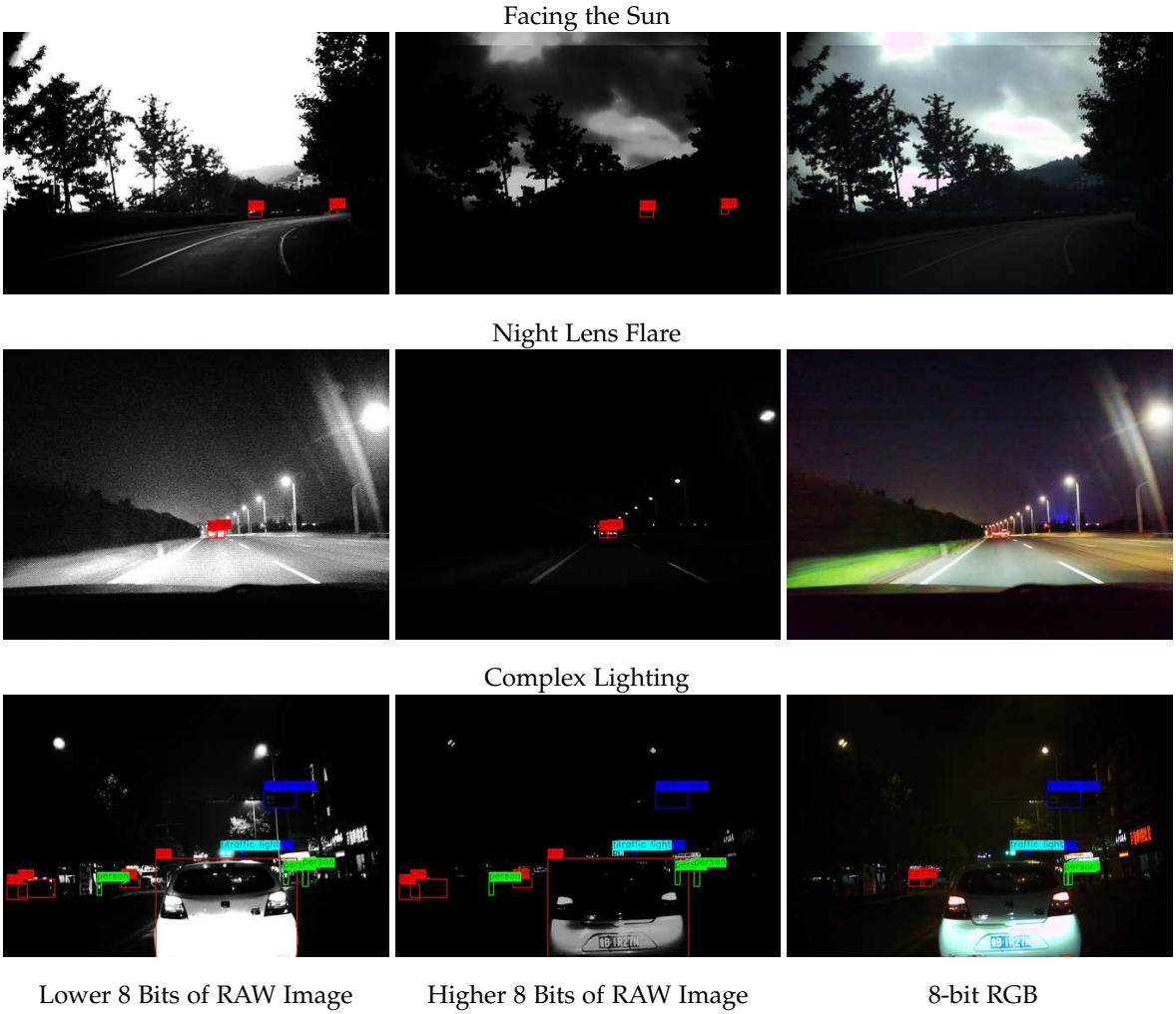

Fig. 10: **Visualizing the detection results under challenging illumination conditions for the RAW domain and RGB domain methods.** The first column displays the lower 8 bits of the RAW data, which retains the shadow details often lost in standard 8-bit RGB images due to brightness clipping. The second (middle) column presents the higher 8 bits of the RAW data, which contains the details in the bright areas. The third column uses the 8-bit RGB for detection. Detection results are overlaid for comparative study.

this way, the ISP modules, which are incorporated into cameras for decades, can be completely bypassed, thus promising an alternative and encouraging paradigm for image/video acquisition, processing, and display. Our Unpaired CycleR2R is able to effectively characterize, embed, and transfer necessary knowledge between unpaired RGB and camera RAW samples to build the mapping between RGB and RAW spaces in an unsupervised manner. This enables us to conveniently generate sufficient simRAW images to retain/finetune popular RGB-domain neural models deployed in existing products for RAW-domain task executions. We present extensive experiments on high-level object detection and low-level image compression tasks in the RAW domain, which show better performance can be achieved in RAW domain compared to the RGB domain. One potential future direction is to develop similar models for processing RAW videos. We will make our MultiRAW dataset and Unpaired CycleR2R code publicly accessible for reproducible research at https://njuvision.github.io/rho-vision upon the acceptance of this work.

8 Acknowledgement

We are very grateful for those pioneering explorations in [14]–[16] which inspire this work.

References

[1] X. Lin, X. Wang, and W. Yang, "From motion to magic: Real-time virtual-real stage effects via 3d motion capture," *Metaverse*, vol. 4, no. 2, 2023. 1

[2] R. Wang and N. Hua, "The image artistry of vr film "killing a superstar"," *Metaverse*, vol. 4, no. 2, 2023. 1

[3] Y. Yang, Z. Hao, W. Peng, K. Tang, and M. Fang, "Multi-task super resolution method for vector field critical points enhancement," *Metaverse*, vol. 3, no. 1, p. 8, 2022. 1

[4] X. Zhang, Y. Zhao, G. Min, W. Miao, H. Huang, and Z. Ma, "Intelligent video ingestion for real-time traffic monitoring," *ACM Trans. Sen. Netw.*, vol. 18, no. 3, sep 2022. 1

[5] T. D. Räty, "Survey on contemporary remote surveillance systems for public safety," *IEEE Transactions on Systems, Man, and Cybernetics, Part C (Applications and Reviews)*, vol. 40, no. 5, pp. 493–515, 2010. 1

[6] R. Okuda, Y. Kajiwara, and K. Terashima, "A survey of technical trend of adas and autonomous driving," in *Technical Papers of 2014 International Symposium on VLSI Design, Automation and Test*. IEEE, 2014, pp. 1–4. 1

[7] D. J. Brady, L. Fang, and Z. Ma, "Deep learning for camera data aquisition, control and image estimation," *Advances in Optics and Photonics*, Sept. 2020. 1

[8] J. Honovich, "Live video monitoring usage statistics," 2015. [Online]. Available: https://ipvm.com/reports/live-video-monitoring-usage-statistics 1

[9] M. Buckler, S. Jayasuriya, and A. Sampson, "Reconfiguring the imaging pipeline for computer vision," in *Proceedings of the IEEE International Conference on Computer Vision*, 2017, pp. 975–984. 1

[10] AI Camera, "Ambarella unveils two new ai chip families for 4k security cameras," 2021. [Online]. Available: https://venturebeat.com/ai/ambarella-unveils-two-new-ai-chip-families-for-4k-security-cameras/ 1

[11] J. Deng, W. Dong, R. Socher, L.-J. Li, K. Li, and L. Fei-Fei, "ImageNet: A Large-Scale Hierarchical Image Database," in *CVPR09*, 2009. 1

[12] J. Redmon, S. Divvala, R. Girshick, and A. Farhadi, "You only look once: Unified, real-time object detection," in *2016 IEEE Conference on Computer Vision and Pattern Recognition (CVPR)*, 2016, pp. 779–788. 2, 6, 7, 8, 11, 12, 14

[13] M. Lu and Z. Ma, "High-efficiency lossy image coding through adaptive neighborhood information aggregation," *arXiv preprint arXiv:2204.11448*, 2022. 2, 9, 10

[14] S. W. Zamir, A. Arora, S. Khan, M. Hayat, F. S. Khan, M.-H. Yang, and L. Shao, "Cycleisp: Real image restoration via improved data synthesis," in *Proceedings of the IEEE/CVF Conference on Computer Vision and Pattern Recognition*, 2020, pp. 2696–2705. 2, 3, 11, 12, 13, 16

[15] M. Afifi, A. Abdelhamed, A. Abuolaim, A. Punnappurath, and M. S. Brown, "CIE XYZ Net: Unprocessing images for low-level computer vision tasks," *IEEE Transactions on Pattern Analysis and Machine Intelligence*, 2021. 2, 3, 6, 11, 12, 13, 16

[16] M. V. Conde, S. McDonagh, M. Maggioni, A. Leonardis, and E. Pérez-Pellitero, "Model-based image signal processors via learnable dictionaries," in *AAAI*, 2022. 2, 3, 4, 11, 12, 13, 16

[17] J.-Y. Zhu, T. Park, P. Isola, and A. A. Efros, "Unpaired image-to-image translation using cycle-consistent adversarial networks," in *Proceedings of the IEEE international conference on computer vision*, 2017, pp. 2223–2232. 2, 3

[18] M. Hnewa and H. Radha, "Multiscale domain adaptive yolo for cross-domain object detection," in *2021 IEEE International Conference on Image Processing (ICIP)*. IEEE, 2021, pp. 3323–3327. 2, 11, 12, 13

[19] Y.-J. Li, X. Dai, C.-Y. Ma, Y.-C. Liu, K. Chen, B. Wu, Z. He, K. Kitani, and P. Vajda, "Cross-domain adaptive teacher for object detection," in *Proceedings of the IEEE/CVF Conference on Computer Vision and Pattern Recognition*, 2022, pp. 7581–7590. 2, 11, 12, 13

[20] H. C. Karaimer and M. S. Brown, "A software platform for manipulating the camera imaging pipeline," in *European Conference on Computer Vision*. Springer, 2016, pp. 429–444. 2

[21] N. A, "Understanding the image signal processor and isp tuning - pathpartnertech." [Online]. Available: https://www.pathpartnertech.com/camera-tuning-understanding-the-image-signal-processor-and-isp-tuning/ 2

[22] R. M. Nguyen and M. S. Brown, "Raw image reconstruction using a self-contained srgb-jpeg image with only 64 kb overhead," in *Proceedings of the IEEE Conference on Computer Vision and Pattern Recognition*, 2016, pp. 1655–1663. 3

[23] T. Brooks, B. Mildenhall, T. Xue, J. Chen, D. Sharlet, and J. T. Barron, "Unprocessing images for learned raw denoising," in *Proceedings of the IEEE Conference on Computer Vision and Pattern Recognition*, 2019, pp. 11 036–11 045. 3, 5

[24] Z. Li, H. Liu, L. Yang, and Z. Ma, "In-camera raw compression: A new paradigm from image acquisition to display," in *54th Asilomar Conference on Signals, Systems and Computers*, 2020. 3

[25] S. Koskinen, D. Yang, and J.-K. Kämäräinen, "Reverse imaging pipeline for raw rgb image augmentation," in *2019 IEEE International Conference on Image Processing (ICIP)*. IEEE, 2019, pp. 2896–2900. 3, 11, 12, 13

[26] T. Plotz and S. Roth, "Benchmarking denoising algorithms with real photographs," in *2017 IEEE Conference on Computer Vision and Pattern Recognition (CVPR)*. Los Alamitos, CA, USA: IEEE Computer Society, jul 2017, pp. 2750–2759. [Online]. Available: https://doi.ieeecomputersociety.org/10.1109/CVPR.2017.294 3

[27] V. Bychkovsky, S. Paris, E. Chan, and F. Durand, "Learning photographic global tonal adjustment with a database of input / output image pairs," in *CVPR 2011*, 2011, pp. 97–104. 3

[28] V. Monga, Y. Li, and Y. C. Eldar, "Algorithm unrolling: Interpretable, efficient deep learning for signal and image processing," *IEEE Signal Processing Magazine*, vol. 38, no. 2, pp. 18–44, 2021. 3, 4

[29] F. Yu, H. Chen, X. Wang, W. Xian, Y. Chen, F. Liu, V. Madhavan, and T. Darrell, "Bdd100k: A diverse driving dataset for heterogeneous multitask learning," in *Proceedings of the IEEE/CVF Conference on Computer Vision and Pattern Recognition*, 2020, pp. 2636–2645. 3, 10, 11

[30] A. Abdelhamed, M. A. Brubaker, and M. S. Brown, "Noise flow: Noise modeling with conditional normalizing flows," in *Proceedings of the IEEE/CVF International Conference on Computer Vision*, 2019, pp. 3165–3173. 3

[31] N. Ohta and A. Robertson, "Cie standard colorimetric system," *Colorimetry: Fundamentals and applications*, pp. 63–114, 2006. 3

[32] J. M. Hollas, *Modern spectroscopy*. John Wiley & Sons, 2004. 4

[33] X. Li, B. Gunturk, and L. Zhang, "Image demosaicing: A systematic survey," in *Visual Communications and Image Processing 2008*, vol. 6822. SPIE, 2008, pp. 489–503. 5

[34] A. Gijsenij, T. Gevers, and J. van de Weijer, "Computational color constancy: Survey and experiments," *IEEE Transactions on Image Processing*, vol. 20, no. 9, pp. 2475–2489, 2011. 5

[35] M. Afifi and M. S. Brown, "What else can fool deep learning? addressing color constancy errors on deep neural network performance," in *2019 IEEE/CVF International Conference on Computer Vision, ICCV 2019, Seoul, Korea (South), October 27 - November 2, 2019*. IEEE, 2019, pp. 243–252. [Online]. Available: https://doi.org/10.1109/ICCV.2019.00033 5

[36] G. D. Finlayson, M. Mackiewicz, and A. Hurlbert, "Color correction using root-polynomial regression," *IEEE Transactions on Image Processing*, vol. 24, no. 5, pp. 1460–1470, 2015. 5

[37] Z. Zhou, N. Sang, and X. Hu, "Global brightness and local contrast adaptive enhancement for low illumination color image," *Optik*, vol. 125, no. 6, pp. 1795–1799, 2014. 5

[38] S. Wolf, *Color correction matrix for digital still and video imaging systems*. National Telecommunications and Information Administration Washington, DC, 2003. 6

[39] H. Farid, "Blind inverse gamma correction," *IEEE transactions on image processing*, vol. 10, no. 10, pp. 1428–1433, 2001. 6

[40] M. Stokes, "A standard default color space for the internet-srgb," *http://www. color. org/contrib/sRGB. html*, 1996. 6, 8

[41] F. Drago, K. Myszkowski, T. Annen, and N. Chiba, "Adaptive logarithmic mapping for displaying high contrast scenes," in *Computer graphics forum*, vol. 22, no. 3. Wiley Online Library, 2003, pp. 419–426. 6

[42] J. T. Barron and Y.-T. Tsai, "Fast fourier color constancy," in *Proceedings of the IEEE conference on computer vision and pattern recognition*, 2017, pp. 886–894. 6

[43] B. Xu, N. Wang, T. Chen, and M. Li, "Empirical evaluation of rectified activations in convolutional network," *arXiv preprint arXiv:1505.00853*, 2015. 6

[44] T. Park, A. A. Efros, R. Zhang, and J.-Y. Zhu, "Contrastive learning for unpaired image-to-image translation," in *European conference on computer vision*. Springer, 2020, pp. 319–345. 6

[45] J. Liu, J. Tang, and G. Wu, "Adadm: Enabling normalization for image super-resolution," *arXiv preprint arXiv:2111.13905*, 2021. 7, 8

[46] T.-Y. Lin, P. Dollár, R. Girshick, K. He, B. Hariharan, and S. Belongie, "Feature pyramid networks for object detection," in *Proceedings of the IEEE CVPR*, 2017, pp. 2117–2125. 6

[47] Q. Chen, Y. Wang, T. Yang, X. Zhang, J. Cheng, and J. Sun, "You only look one-level feature," in *Proceedings of the IEEE/CVF conference on computer vision and pattern recognition*, 2021, pp. 13 039–13 048. 6

[48] R. Girshick, "Fast r-cnn," in *Proceedings of the IEEE international conference on computer vision*, 2015, pp. 1440–1448. 6

[49] S. Ren, K. He, R. Girshick, and J. Sun, "Faster r-cnn: Towards real-time object detection with region proposal networks," *Advances in neural information processing systems*, vol. 28, 2015. 6

[50] Y. Wu and K. He, "Group normalization," in *Proceedings of the European conference on computer vision (ECCV)*, 2018, pp. 3–19. 6, 8

[51] J. Wang, K. Sun, T. Cheng, B. Jiang, C. Deng, Y. Zhao, D. Liu, Y. Mu, M. Tan, X. Wang *et al.*, "Deep high-resolution representation learning for visual recognition," *IEEE transactions on pattern analysis and machine intelligence*, vol. 43, no. 10, pp. 3349–3364, 2020. 7

[52] S. Ioffe and C. Szegedy, "Batch normalization: Accelerating deep network training by reducing internal covariate shift," in *Interna-*

tional conference on machine learning. PMLR, 2015, pp. 448–456. 8
[53] Y. Liu, J. Ge, C. Li, and J. Gui, "Delving into variance transmission and normalization: Shift of average gradient makes the network collapse," *arXiv preprint arXiv:2103.11590*, 2021. 8
[54] T. Chen, H. Liu, Z. Ma, Q. Shen, X. Cao, and Y. Wang, "End-to-end learnt image compression via non-local attention optimization and improved context modeling," *IEEE Trans. Image Processing*, vol. 30, pp. 3179–3191, 2021. 9
[55] M. Lu, P. Guo, H. Shi, C. Cao, and Z. Ma, "Transformer-based image compression," *IEEE Data Compression Conf.*, Jan. 2022. 9
[56] J. Liu, C.-H. Wu, Y. Wang, Q. Xu, Y. Zhou, H. Huang, C. Wang, S. Cai, Y. Ding, H. Fan *et al.*, "Learning raw image denoising with bayer pattern unification and bayer preserving augmentation," in *Proceedings of the IEEE Conference on Computer Vision and Pattern Recognition Workshops*, 2019, pp. 0–0. 9
[57] F. Mentzer, E. Agustsson, M. Tschannen, R. Timofte, and L. V. Gool, "Practical full resolution learned lossless image compression," in *Proceedings of the IEEE/CVF conference on computer vision and pattern recognition*, 2019, pp. 10 629–10 638. 10
[58] S. Cao, C.-Y. Wu, and P. Krähenbühl, "Lossless image compression through super-resolution," *arXiv preprint arXiv:2004.02872*, 2020. 10
[59] F. Mentzer, E. Agustsson, M. Tschannen, R. Timofte, and L. V. Gool, "Practical full resolution learned lossless image compression," in *Proceedings of the IEEE/CVF conference on computer vision and pattern recognition*, 2019, pp. 10 629–10 638. 10
[60] S. Cao, C.-Y. Wu, and P. Krähenbühl, "Lossless image compression through super-resolution," *arXiv preprint arXiv:2004.02872*, 2020. 10
[61] M. Sandler, A. Howard, M. Zhu, A. Zhmoginov, and L.-C. Chen, "Mobilenetv2: Inverted residuals and linear bottlenecks," in *Proceedings of the IEEE conference on computer vision and pattern recognition*, 2018, pp. 4510–4520. 11, 12, 14
[62] Y. Chen, W. Li, C. Sakaridis, D. Dai, and L. Van Gool, "Domain adaptive faster r-cnn for object detection in the wild," in *Proceedings of the IEEE conference on computer vision and pattern recognition*, 2018, pp. 3339–3348. 11, 12, 13
[63] J. Liu, G. Lu, Z. Hu, and D. Xu, "A unified end-to-end framework for efficient deep image compression," *arXiv preprint arXiv:2002.03370*, 2020. 10, 11, 13
[64] H. Danyali and A. Mertins, "Highly scalable image compression based on spiht for network applications," in *Proceedings. International Conference on Image Processing*, vol. 1, 2002, pp. I–I. 15

Zhihao Li (Member, IEEE) received his B.S. and Master degrees in the School of Electronic Science and Engineering from Nanjing University, Jiangsu, China, in 2020 and 2023 respectively. His current research focuses on raw image signal processing and event camera. He is a co-recipient of the 2nd International Illumination Estimation Challenge and the CVPRW 2022 Night Image Rendering Challenge Runner-up solution.

Ming Lu (Member, IEEE) is an Associate Researcher in the School of Electronic Science and Engineering, Nanjing University, Jiangsu, China. He received his B.S. and Ph.D. degrees in the School of Electronic Science and Engineering from Nanjing University, Jiangsu, China, in 2016 and 2023 respectively. His current research focuses on deep learning-based image/video coding. He is a co-recipient of the 2018 ACM SIGCOMM Student Research Competition Finalist, the 2020 IEEE MMSP Image Compression Grand Challenge Best Performing Solution, and the 2023 IEEE WACV Best Algorithms Paper Award.

Xu Zhang (Member, IEEE) is a Lecturer with the School of Computing, Faculty of Engineering and Physical Sciences, University of Leeds, LS2 9JT, United Kingdom. He received the BS degree in communication engineering from the Beijing University of Posts and Telecommunications, China, in 2012 and the Ph.D. degree in computer science from the Department of Computer Science and Technology, Tsinghua University, China, in 2017. He worked at Nanjing University and the University of Exeter before joining the University of Leeds. His research interests include AI for computing and networking, multimedia communication, and Internet of Things. He was a recipient of the EU Marie Skłodowska-Curie Individual Fellowships and a co-recipient of the 2019 IEEE Broadcast Technology Society Best Paper Award.

Xin Feng (Senior Member, IEEE) received her B.S. degree in computer science and technology from Chongqing University in 2004. She conducted her postgraduate study from 2004 to 2006 and got the Ph.D. degree in computer applications from Chongqing University in 2011. She is currently an associate professor at Chongqing University of Technology. She studied at New York University as a postdoctoral from 2014 to 2016. Her research falls in the area of computer vision, image, and video processing. Her current research interests cover object detection, and multi-object tracking for visual perception in auto-driving.

M. Salman Asif (Senior Member, IEEE) received the B.Sc. degree from the University of Engineering and Technology, Lahore, Pakistan, and the M.S and Ph.D. degrees from the Georgia Institute of Technology, Atlanta, GA, USA. He is currently an associate professor with the University of California Riverside, Riverside, CA, USA. Prior to that, he was a Postdoctoral Researcher with Rice University, Houston, TX, USA, and a Senior Research Engineer with Samsung Research America, Dallas. His research interests include computational imaging, signal/image processing, computer vision, and machine learning. He was the recipient of the NSF CAREER Award, Google Faculty Award, Hershel M. Rich Outstanding Invention Award, and UC Regents Faculty Fellowship and Development Awards.

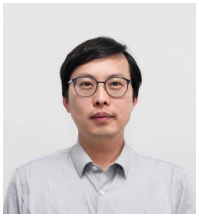

Zhan Ma (Senior Member, IEEE) is a Professor in the School of Electronic Science and Engineering, Nanjing University, Jiangsu, 210093, China. He received his Ph.D. from New York University, New York, in 2011 and his B.S. and M.S. from the Huazhong University of Science and Technology, Wuhan, China, in 2004 and 2006 respectively. From 2011 to 2014, he has been with Samsung Research America, Dallas, TX, and Futurewei Technologies, Inc., Santa Clara, CA, respectively. His research focuses include learned image/video coding and computational imaging. He was awarded the 2018 PCM Best Paper Finalist, the 2019 IEEE Broadcast Technology Society Best Paper Award, the 2020 IEEE MMSP Grand Challenge Best Image Coding Solution, the 2023 IEEE WACV Best Algorithms Paper Award, and the 2023 IEEE Circuits and Systems Society Outstanding Young Author Award.

Supplemental Materials - Efficient Visual Computing with Camera RAW Snapshots

Zhihao Li, Ming Lu, Xu Zhang, Xin Feng, M. Salman Asif, and Zhan Ma

arXiv:2212.07778v2 [cs.CV] 25 Jan 2024

***Abstract*—In this supplementary material, we provide additional information to further evidence the generalization of the proposed ρ-*Vision* for various functionalities. Specifically, we first compare the RGB-Vision and ρ-Vision frameworks using a real-world hardware implementation in Sec. S.I. Then, we provide details of our Unpaired CycleR2R in Sec. S.II and give proofs of some equations in Sec. S.III. In addition, we demonstrate the advantages of running classification and segmentation in the RAW domain directly in Sec. S.IV and Sec. S.V, respectively. At last, we show more visualization results in Sec. S.VI.**

***Index Terms*—Camera RAW, RAW-domain Object Detection, RAW Image Compression**

S.I. A Real-World Hardware Implementation

A. Hardware System for Comparative Benchmark

A commodity hardware platform is used to assess the efficiency of RAW-domain visual computing as illustrated in Fig. S1a. It is built upon the Axera-Tech AX620A SoC with a quad-core Arm Cortex-A7 processor, an NPU (Neural Processing Unit), an ISP (Image Signal Processor), and other subsystems. This AX620A SoC is primarily used to process images and videos for vision tasks. Its ISP has two modes: one is the Standard mode (AX620A ISP), and the other is the AI mode (AX620A AI ISP). When using AX620A AI ISP, onboard NPU is utilized to run various neural algorithms like NN (Neural Network) denoising, by which AX620A SoC claims its outstanding performance for low-light imaging.

We use the same RAW samples in the MultiRAW dataset for a fair evaluation. The YOLOv8-S, recommended by the AX620A SoC specification, exemplifies the detection task. Its default settings are assumed for consistency and reproducibility. Upon completing the training of YOLOv8-S, its model is quantized into INT-8 precision using AX620A's official quantization tool and subsequently deployed on AX620A's NPU for inference.

Metrics such as mAP, latency, power consumption, and memory usage are collected for quantitative comparison. With this aim, when executing the YOLOv8-S, a UC96B power meter is connected to the AX620A SoC to collect the power usage, latency is measured using a timer library (C++), and the memory consumption is reported using the default memory monitoring tool provided by the AX620A SoC.

- **ρ-Vision** trains YOLOv8-S using RAW samples (from the iPhone XSmax, a subset of the MultiRAW dataset). Then, such a RAW-domain YOLOv8-S is quantized using the abovementioned rules and deployed on the NPU for detection. For task inference, RAW images are fed directly to the neural model (without requiring ISP computations). Following the common practice, 70 % RAW images are used to train RAW-domain YOLOv8-S, and the remaining 30 % RAW images are tested using quantized YOLOv8-S on NPU. Fig. S1b plots the processing steps in ρ-Vision.
- **RGB-Vision** applies the AX620A ISP onboard to convert RAW images to their corresponding RGB formats for subsequent computations. The training and testing split is the same as in the ρ-Vision paradigm. The RGB-vision

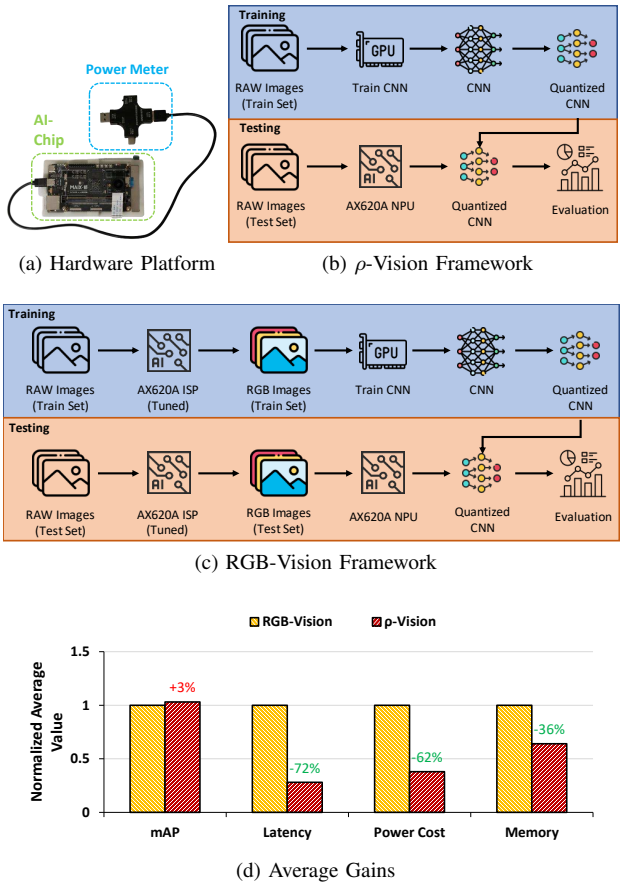

(a) Hardware Platform (b) ρ-Vision Framework

(c) RGB-Vision Framework

(d) Average Gains

Fig. S1: **RGB-Vision vs. ρ-Vision.** (a) The hardware system uses AX620A AI SoC. A UC96B power meter is connected for measurement; (b) ρ-Vision framework trains and tests models using RAW images directly, completely bypassing the ISP; (c) Traditional RGB-Vision framework requires the ISP to generate RGB images for model training and testing; (d) **Average Gains of ρ-Vision to RGB-Vision.** Metrics are normalized to the results generated by the RGB-Vision pipeline.

iPhone → AX620A (D) | iPhone → AX620A (T) | AX620A (T) → AX620A (T) | iPhone → iPhone

Fig. S2: **Impact of ISP used in RGB-Vision on the detection task.** The setup of "Training ISP→Testing ISP" indicates the "Training ISP" used to generate RGB images for training and the "Testing ISP" used to generate RGB images for testing respectively. Default parameters used by the ISP are marked with "(D)" and expert-tuned parameters used by the ISP are annotated with "(T)". The first two columns illustrate domain discrepancies when training and testing using different ISPs, while the last two columns demonstrate how ISP quality (with expert tuning) affects object detection accuracy. *Zoom for better details.*

TABLE S1: Detection performance for various ISP combinations.

Domain	Training ISP	Testing ISP	Car	Person	Traffic Light	Traffic Sign	mAP
RGB-Vision	iPhone	AX620A (Default)	0.324	0.022	0.134	0.213	0.173
	iPhone	AX620A (Tuned)	0.696	0.108	0.523	0.253	0.397
	AX620A (Tuned)	AX620A (Tuned)	0.788	0.225	0.661	0.443	0.529
	iPhone	iPhone	**0.798**	0.219	**0.693**	0.474	**0.546**
ρ-Vision	-	-	0.796	**0.241**	0.655	**0.490**	**0.546**

processing pipeline is pictured in Fig. S1c.

All associated hardware drivers, system images, benchmark code, and datasets will soon be available at https://njuvision.github.io/rho-vision to encourage reproducible research.

B. Experimental Analysis

Overall Evaluation. Fig. S1d showcases the efficacy of the proposed ρ-Vision paradigm. Compared to RGB-Vision, it provides a notable 3 % detection accuracy increase. The same YOLOv8-S is just retrained using RAW images without any dedicated network model engineering. It reduces the latency by 72 %, a critical advancement for autonomous driving applications. Furthermore, the 62 % reduction in power consumption presents significant advantages of ρ-Vision for AIoT devices, where energy efficiency is crucial. The 36 % decrease in memory usage also enables the deployment of ρ-Vision on lower-cost embedded devices. The performance improvement owes to better-preserving scene information in the RAW domain. The skipping of ISP generally avoids the extra computations and memory caching, leading to a noticeable cost and latency reduction. These promise the encouraging potential of ρ-Vision in advancing computer vision applications for better task performance, faster response, and less cost.

Impact of ISP used in RGB-Vision Paradigm. In Fig. S1c, the AX620A ISP is expert-tuned. This is because default settings used in AX620A ISP cannot provide a decent result, which motivates us to study the impact of various ISP configurations on task efficiency. The ISP used in the iPhone XSmax is also evaluated as Apple experts deliberately calibrate it for outstanding quality. Note that the ISP is only required in the RGB-Vision framework.

Similarly, we use iPhone RAW images from the MultiRAW dataset in experiments. We have different ISP combinations for RGB-Vision to train and test RGB images (converted from the

same set of iPhone RAWs). The training and testing split is the same for either RGB-domain or RAW-domain processing.

As in Table S1 for the RGB-Vision category, the training ISP converts iPhone RAW images to the corresponding RGB samples to train YOLOv8-S, while the testing ISP is used to generate RGB samples (from iPhone RAW images) for testing previously trained YOLOv8-S.

The setup using the same iPhone ISP to generate RGB images for training and testing provides the best performance (see the last row of RGB-Vision in Table S1). Although we have tried our best to fine-tune the AX620A ISP to mimic the iPhone ISP, the setup using the same AX620A ISP (Tuned) to generate RGB images for training and testing is inferior to the case using the iPhone ISP that is deliberately calibrated by Apple imaging experts, e.g., 0.529 vs. 0.546 mAP. The detection performance is sharply degraded if we use different ISPs to generate training and testing RGB samples (see 1st and 2nd rows of Table S1 in RGB-Vision), suggesting that the ISP configuration is vital for task performance.

Fig. S2 visualizes detection results on testing images, further confirming the observations in Table S1 where inappropriate use of ISPs would lead to catastrophic performance degradation (see missing objects in the first column).

By contrast, under the ρ-Vision setup, YOLOv8-S is trained and tested on iPhone RAW images directly. The average detection performance is the same as using the iPhone ISP for both training and testing in RGB-vision. More importantly, expert tuning or dedicated calibration of ISP is no longer required. All of these suggest the encouraging prospects of using ρ-Vision in vision tasks.

Challenging Imaging Conditions are additionally examined to compare the efficiency of ρ-Vision and RGB-Vision pipelines. Two representative contexts are considered: the low-light illumination with high-noise levels and the scenario with high dynamic range (HDR) conditions.

Low-light illumination with high noise scenario is evaluated with object classification. We closely follow [*S1*] to perform the task, which involves training a MobileNet-V1 using noise-augmented ImageNet samples, then testing real-world noisy images acquired using a Google Pixel camera under low-light/high-noise conditions.

As for RGB-Vision, we directly train an RGB-domain MobileNet-V1 using the ImageNet dataset (RGB_{IN}) (with noise augmentation). In the meantime, we respectively use AX620A ISP and AX620A AI-ISP to transform RAW images acquired using Google Pixel camera (RAW_{GP}) to the corresponding RGB datasets, e.g., RGB_{AX} and $\text{RGB}_{\text{AX}-\text{AI}}$ to test aforementioned RGB-domain MobileNet-V1.

As for ρ-Vision, we first train our Unpaired CycleR2R model using clean RAW and RGB images from the Google Pixel and ImageNet datasets, i.e., RAW_{GP} and RGB_{IN}, respectively. Then, we use the invISP module in this Unpaired CycleR2R to convert RGB images in ImageNet to simulated RAW samples, i.e., $\text{simRAW}_{\text{IN}}$, to train the RAW-domain MobileNet-V1. The same noise augmentation is performed upon $\text{simRAW}_{\text{IN}}$. Such a RAW-domain MobileNet-V1 tests RAW samples directly from RAW_{GP}.

Evaluations presented in Table S2 clearly evidence the superiority of ρ-Vision paradigm. Notable reductions are reported for power consumption, memory footprint, and computational latency, owing to removing the ISP subsystem in the proposed ρ-Vision framework.

ρ-Vision only requires 0.006 J for task inference, compared to 0.128 and 0.162 J consumed by RGB-Vision methods using AX620A ISP and AX620A AI ISP. Furthermore, it exhibits the lowest latency at 2.71 ms, a substantial decrease from the 48.65 ms and 64.75 ms observed with the methods using AX620A ISP and AX620A AI ISP. This is because small-size images, e.g., 224×224, are used in the classifier, but ISPs must process images with the original resolution (2560×1440). Such a sharp increase in data volume increases power consumption, memory footprint, and latency.

ρ-Vision also presents better classification accuracy. We attribute it to noise separation and suppression in the RAW domain being more tractable than in the RGB domain (after a serial nonlinear transformation) [*S1*].

Notably, the AX620A AI ISP does not enhance classification performance under such extreme low-light conditions, as AX620A AI ISP models are typically trained for some specific cameras and may not generalize well to a new camera from the above discussions.

HDR conditions are studied with the detection task. 24-bit LUCID TRI054S RAW images (RAW_{LT}) covering the tunnel exit scenes are used. These HDR scenes are often encountered when driving through the tunnel and simultaneously experiencing extraordinarily bright and dark regions.

As for ρ-Vision, we train the RAW-domain detector (YOLOv8-S) using RAW_{LT}. In contrast, RAW samples in $\text{RAW}_{\text{LT}}$are first converted to RGB counterparts using the AX620A ISP to train the RGB-domain detector used in the RGB-Vision framework.

Besides the reductions in power consumption, memory footprint, and latency, the ρ-Vision framework achieves superior mAP across all categories, particularly in detecting traffic lights and signs (e.g., labeled as "Tr. L." and "Tr. S.") in Table S3. The improvement in mAP indicates the enhanced capability of the ρ-Vision to discern features in HDR conditions. This is essential for applications such as autonomous driving, where accurate and prompt traffic detection is crucial.

The combination of reduced latency, lower power consumption, and memory usage, along with higher mAP scores, affirms the effectiveness of the ρ-Vision framework in challenging HDR scenarios, highlighting its potential for real-world applications where both performance and efficiency are of paramount importance.

S.II. Details of the Unpaired CycleR2R

A. Architecture of Basic Neural Network

Table S4 details the architecture of the basic neural network $E(\cdot)$ used in Unpaired CycleR2R. This basic network $E(\cdot)$ consists of five layers in total and is used for IEM (Illumination Estimation Module), AWB (Auto White Balance), BA (Brightness Adjustment), and CC (Color Correction). The first layer applies the 5×5 convolution with 32 channels, and the

TABLE S2: **Classification Accuracy of RGB-Vision and ρ-Vision Frameworks Under Low-Light Conditions.** Latency measures the total processing duration by both the ISP and model, as well as the power consumption (Power.) and memory requirements (Mem.) for each method, besides the Top-1 classification accuracy (Acc.). *The results of Google Pixel ISP are copied from the paper [*S1*]. The "invISP" is used in ρ-Vision to generate simulated RAW samples to train the classifier, while RGB-vision methods do not require this step. RGB-Vision methods train the RGB-domain classifier using RGB images from the ImageNet dataset (RGB_{IN}) while ρ-Vision trains the RAW-domain classifier using simulated RAW images generated using the invISP. RAW images acquired by Google Pixel (RAW_{GP}) [*S1*] under extreme low-light conditions are used for evaluation. In the RGB-Vision pipeline, these RAW images are converted using different ISPs to RGB samples for using the RGB-domain classifier, while in the ρ-vision paradigm, these RAW images are directly fed to the RAW-domain classifier.

Method	**invISP**	**Classifier**		**Latency**		**Power.**	**Mem.**	**Acc.**
	Train	**Train**	**Test**	**ISP**	**Model**			
RGB-Vision w/ AX620A ISP	-	RGB_{IN}	RGB_{AX}	48.65 ms	2.73 ms	0.128 J	65 MB	0.0
RGB-Vision w/ AX620A AI-ISP	-	RGB_{IN}	$\text{RGB}_{\text{AX-AI}}$	64.75 ms	4.36 ms	0.162 J	81 MB	0.0
RGB-Vision w/ *Google Pixel ISP	-	RGB_{IN}	RGB_{GP}	-	-	-	-	1.4
ρ-Vision	RGB_{IN}, RAW_{IN}	$\text{simRAW}_{\text{IN}}$	RAW_{GP}	**0 ms**	**2.71 ms**	**0.006 J**	**25 MB**	**19.8**

TABLE S3: **Comparative Analysis of RGB-Vision and ρ-Vision Frameworks in High Dynamic Range (HDR) Scenarios.** The RAW-domain detector is calibrated with 24-bit LUCID TRI054S RAW images (RAW_{LT}). The RGB-domain detector is trained and evaluated on RGB images generated using AX620A ISP (RGB_{AX}). Latency encompasses the total processing time of both the ISP and the detection model. We present the power consumption (Power.) and memory footprint (Mem.) alongside the mean Average Precision (mAP). Abbreviations "Tr. L." and "Tr. S.", denote traffic light and traffic sign, respectively.

Framework	**Detector**		**Latency**		**Power.**	**Mem.**	$\textbf{AP}_{\textbf{Car}}$	$\textbf{AP}_{\textbf{Tr. L}}$	$\textbf{AP}_{\textbf{Tr. S}}$	**mAP**
	Train	**Test**	**ISP**	**Model**						
RGB-Vision	RGB_{AX}	RGB_{AX}	48.55 ms	**17.07 ms**	0.152 J	55 MB	81.3	27.9	61.2	56.8
ρ-Vision	RAW_{LT}	RAW_{LT}	**0 ms**	18.18 ms	**0.058 J**	**35 MB**	**84.8**	**35.5**	**69.7**	**63.3**

subsequent two layers use 3×3 convolutions and 64 channels. The final two layers use simple linear layers instead.

The example of "Conv: k5c32s2" stands for a convolutional layer having convolutions with spatial kernel size at 5×5 (k5), 32 channels (c32), and a stride of two based spatial downsampling (s2) at both dimensions. The same convention is applied to the linear layer (Linear) and average pooling layer (Avg Pool). "Leaky RELU" [*S4*] is used as the activation, and "Mean" stands for the average operator in the spatial domain for each channel. Considering the output channel of $E(\cdot)$ is specific for different purposes across aforementioned modular components, we mark it using a predefined variable C_{out}.

B. Architectures of Discriminators

As in the main paper, D_{color} and D_{bright} are applied to measure the similarity between generated and real images. D_{color} stacks five convolutional layers with Leaky ReLU [*S4*] and D_{bright} uses five linear layers instead to process 1D grayscale histogram. Details of kernel size, channels, and strides are listed in Tabel. S4.

C. Gamma Correction Standard

Gamma correction matches the non-linear characteristics of a display device or human perception [*S3*]. We adopt the correction function recommended in ITU-R BT. 709 standard [*S4*], noted as f_g, which is widely used in commodity ISPs today [*S4*].

$$\begin{aligned}\boldsymbol{y} &= f_g \circ \boldsymbol{x}_{cc} \\ &= \begin{cases} 12.92 \cdot \boldsymbol{x}_{cc}, & \boldsymbol{x}_{cc} \leq 0.00304, \\ 1.055 \cdot \boldsymbol{x}_{cc}^{1/2.4} - 0.055, & \boldsymbol{x}_{cc} > 0.00304. \end{cases}\end{aligned} \tag{S1}$$

Correspondingly, the inverse function g_g is:

$$\begin{aligned}\boldsymbol{x}_{cc} &= g_g \circ \boldsymbol{x}_g \\ &= \begin{cases} \dfrac{\boldsymbol{y}}{12.92}, & \boldsymbol{y} \leq 0.04045, \\ \left(\dfrac{\boldsymbol{y} + 0.055}{1.055}\right)^{2.4}, & \boldsymbol{y} > 0.04045. \end{cases}\end{aligned} \tag{S2}$$

S.III. Details of *Distribution Analysis of RAW images*

A. The proof of the equation (28)

We start from the loss function $\mathcal{L}$:

$$\mathcal{L} = \frac{1}{H \times W} \left(\boldsymbol{w} * (\boldsymbol{P} - 0.5) + \mathbf{b} - \hat{\mathbf{y}}\right)^2, \tag{S3}$$

where $\boldsymbol{w} \in \mathbb{R}^{S \times S}$ is the convolution kernel with kernel size S.

Then the partial derivative of $w \in \boldsymbol{w}$ could be formulated as:

$$\frac{\partial \mathcal{L}}{\partial w} = \frac{1}{H \times W} \sum_{j=0}^{H} \sum_{i=0}^{W} 2 \left(\mathbf{y}_{ij} - \hat{\mathbf{y}}\right) \left(\mathbf{x}_{ij+mn} - 0.5\right) \tag{S4}$$

where $\mathbf{x}_{ij+mn} \in \boldsymbol{P}$ and mn is the shift position of w according to the kernel center of $\boldsymbol{w}$. $\mathbf{y}_{ij}$ is the convolution output at position ij. To calculate $\mathbf{y}_{ij}$, we define $\boldsymbol{x}_{ij}^{w}$ as a window of $\boldsymbol{P}$ with the same size of $\boldsymbol{w}$ located at ij. Considering the similarity among adjacent pixels, for a neighborhood pixel of $\mathbf{x}_{ij}$, *i.e.*, $\mathbf{x}_{neibor} \in \boldsymbol{x}_{ij}^{w}$, we have $\mathbf{x}_{neibor} = \mathbf{x}_{ij} + \delta$, where δ follows a Gaussian distribution with zero mean. Thus, $\mathbf{y}_{ij}$ could be expanded as:

$$\mathbf{y}_{ij} = (\mathbf{x}_{ij} - 0.5) \sum w + + \sum w\delta. \tag{S5}$$

For simplify, we use $\tilde{\boldsymbol{x}}$ and $\tilde{\mu}$ to replace $\boldsymbol{x} - 0.5$ and $\mu - 0.5$, respectively. Besides, we set $A = \sum w,\ B = + \sum w\delta,\ C = 2A,\ D = 2\left(B - \hat{\mathbf{y}}\right)$. Having $\mathbf{y}_{ij} = A\tilde{\mathbf{x}} + B$, the $\frac{\partial \mathcal{L}}{\partial w}$ will be:

$$\begin{aligned}
\frac{\partial \mathcal{L}}{\partial w} &= 2\mathbb{E}\left[\left(\mathbf{y} - \hat{\mathbf{y}}\right)(\mathbf{x} - 0.5)\right] \\
&= 2\mathbb{E}\left[\left(A\tilde{\mathbf{x}} + B - \hat{\mathbf{y}}\right)\tilde{\mathbf{x}}\right] \\
&= 2\mathbb{E}\left[A\tilde{\mathbf{x}}^2 + (B - \hat{\mathbf{y}})\tilde{\mathbf{x}}\right] \\
&= 2\mathbb{E}\left[A\right]\mathbb{E}\left[\tilde{\mathbf{x}}^2\right] + 2(\mathbb{E}\left[B\right] - \hat{\mathbf{y}})\mathbb{E}\left[\tilde{\mathbf{x}}\right] \\
&= 2A(\tilde{\mu}^2 - \sigma^2) + 2(b - \hat{\mathbf{y}})\tilde{\mu} \\
&= C(\tilde{\mu}^2 - \sigma^2) + D\tilde{\mu}.
\end{aligned} \tag{S6}$$

Since μ and σ are independent and we only concern with the impact of $p\left(\mu\right)$, we set Var $\left[\sigma^2\right]$ to a constant. Then the variance could be expanded as:

$$\begin{aligned}
\text{Var}\left[\frac{\partial \mathcal{L}}{\partial w}\right] &= \text{Var}\left[C\tilde{\mu}^2 + D\tilde{\mu}\right] + \text{Var}\left[C\sigma^2\right] \\
&= \mathbb{E}\left[\left(C\tilde{\mu}^2 + D\tilde{\mu}\right)^2\right] - \mathbb{E}\left[C\tilde{\mu}^2 + D\tilde{\mu}\right]^2 \\
&\quad + \text{const} \\
&= \mathbb{E}\left[C^2\tilde{\mu}^4\right] + \cancel{\mathbb{E}\left[CD\tilde{\mu}^3\right]} + \mathbb{E}\left[D^2\tilde{\mu}^2\right] \\
&\quad - \left(\mathbb{E}\left[C\tilde{\mu}^2\right] + \cancel{\mathbb{E}\left[D\tilde{\mu}\right]}\right)^2 + \text{const} \\
&= \mathbb{E}\left[\left(C\tilde{\mu}^2\right)^2\right] - \left(\mathbb{E}\left[C\tilde{\mu}^2\right]\right)^2 \\
&\quad + \mathbb{E}\left[\left(D\tilde{\mu}\right)^2\right] - \left(\mathbb{E}\left[D\tilde{\mu}\right]\right)^2 + \text{const} \\
&= \text{Var}\left[C\tilde{\mu}^2\right] + \text{Var}\left[D\tilde{\mu}\right] + \text{const} \\
&= C^2\text{Var}\left[\tilde{\mu}^2\right] + D^2\text{Var}\left[\tilde{\mu}\right] + \text{const}.
\end{aligned} \tag{S7}$$

TABLE S4: Network settings of Unpaired CycleR2R.

Basic Encoder $E\left(\cdot\right)$	Discriminator D_{color}	Discriminator D_{bright}
Conv: k5c32s2	Conv: k4c64s2	Linear: c1024
Leaky RELU	Leaky RELU	Leaky RELU
Avg Pool: s2	Conv: k4c128s2	Linear: c1024
Conv: k3c64s2	Leaky RELU	Leaky RELU
Leaky RELU	Conv: k4c256s2	Linear: c256
Avg Pool: s2	Leaky RELU	Leaky RELU
Conv: k3c64s1	Conv: k4c512s2	Linear: c256
Leaky RELU	Leaky RELU	Leaky RELU
Mean	Conv: k4c1s2	Linear: c1
Linear: c256	Mean	-
Linear: cC_{out}	-	-

B. *The proof of the equation* (29)

Given the μ following the distribution in (25), the Var $[\tilde{\mu}]$ could be written as:

$$\begin{aligned}
\text{Var}\left[\tilde{\mu}\right] &= \text{Var}\left[\mu - 0.5\right] = \text{Var}\left[\mu\right] \\
&= \int_0^1 \left[\mu - \mathbb{E}\left(\mu\right)\right]^2 p\left(\mu\right) \mathrm{d}\mu \\
&= \int_0^1 \left(\mu - 0.5\right)^2 \left(k\mu^2 - k\mu + \frac{k}{6} + 1\right)\mathrm{d}\mu \\
&= F(\mu = 1) - F(\mu = 0) \\
&= \left(\frac{1}{21} - \frac{k}{720}\right) - \left(-\frac{k}{144} - \frac{1}{24}\right) \\
&= \frac{k}{180} + \frac{1}{12},
\end{aligned} \tag{S8}$$

where $F\left(\mu\right) = k\left(\frac{\mu^5}{5} - \frac{\mu^4}{2} + \frac{\mu^3}{12} - \frac{\mu^2}{8}\right) + \frac{k}{18}\left(\mu - \frac{1}{2}\right)^3$.

Thus, Var $\left[\frac{\partial \mathcal{L}}{\partial w}\right]$ will be:

$$\begin{aligned}
\text{Var}\left[\frac{\partial \mathcal{L}}{\partial w}\right] &\approx D^2\text{Var}\left[\tilde{\mu}\right] + \text{const} \\
&= D^2\left(\frac{k}{180} + \frac{1}{12}\right) + \text{const} \\
&= D^2\frac{k}{180} + \text{const}.
\end{aligned} \tag{S9}$$

S.IV. RAW-DOMAIN CLASSIFICATION

In this section, we present the application of our Unpaired CycleR2R model for the classification task in the RAW domain.

A. *Datasets and Baselines*

We utilize the identical dataset for training and testing as in [*S1*]. For generating the training set, we use ImageNet [*S3*] to generate simulated RAW images with noises. As for testing, a real-world RAW dataset captured by a Google Pixel camera, e.g., RAW_{GP}, is used. This dataset collects images acquired with low-light conditions spanning a range of illumination from 1 lux to 200 lux and containing 1103 images in 40 categories.

We employed the MobileNet-V1 [*S4*] for classification as suggested by [*S1*].

As for the proposed ρ-Vision, Unpaired CycleR2R is first trained using RGB images in ImageNet (RGB_{IN}) and Google Pixel RAWs (RAW_{GP}) to generate a simulated RAW dataset ($\text{simRAW}_{\text{IN}}$). This $\text{simRAW}_{\text{IN}}$ is augmented with noises and applied to train the RAW-domain classifier MobileNet-V1. Consequently, the trained RAW-domain MobileNet-V1 examines the testing RAWs from RAW_{GP} for task inference.

As for the Anscombe ISP method proposed in [*S1*], ImageNet RGB images (RGB_{IN}) undergo mosaic operations to generate simulated RAWs, which are then injected with Gaussian-Poisson noise to produce noisy simRAWs. The training has two steps: First, the Anscombe ISP is trained with paired noisy RAW and clean RGB images. Second, Anscombe ISP and Imagenet pre-trained MoblieNet-V1 are jointly trained using noisy simRAWs and classification label annotations. During the testing, the Anscombe ISP converts Google Pixel

TABLE S5: **Classification Accuracy On Google Pixel RAW images.**

Method	invISP	Classifier		Top-1 Acc.	Top-5 Acc.	# Parameters	FLOPs
	Train	Train	Test				
Anscombe ISP*[*S1*]	-	$RGB_{Ans\text{-}ISP}$	$RGB_{Ans\text{-}ISP}$	33.1	58.4	4.28	282
Mosaic RAW*[*S1*]	-	$simRAW_{IN}$	RAW_{GP}	27.0	52.5	**4.23**	**181**
Unpaired CycleR2R	RGB_{IN}, RAW_{GP}	$simRAW_{IN}$	RAW_{GP}	**35.5**	**72.1**	**4.23**	**181**

* Both the Anscombe ISP and Mosaic RAW apply simple mosaic operations to generate RAW samples from the corresponding RGB images. They don't need to train the invISP.

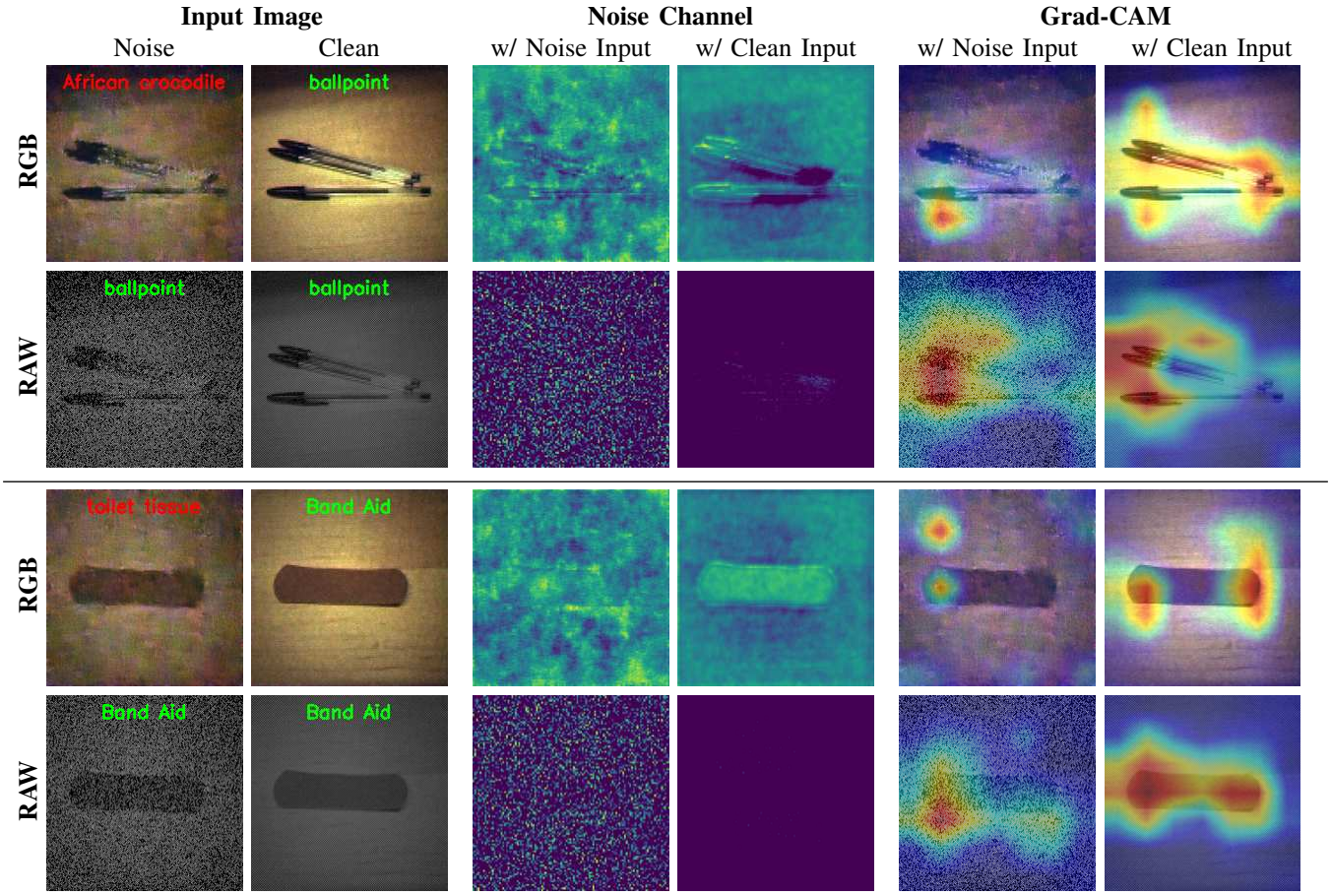

Fig. S3: **Visualization of Classifier Response to Noisy and Clean Inputs** The "RGB" rows represent the processing using the Anscombe ISP [*S1*] where it inputs the RGB image for classification; In contrast, the "RAW" rows stand for the processing using Unpaired CycleR2R where the RAW images are directly processed. Noise is augmented upon the clean inputs to form Noisy samples. The "Noise Channel" is the feature channel in the shallow layer "Conv2d_0" that presents the maximum difference when processing the noise and clean inputs respectively. The Grad-CAM [*S2*] visualizations are based on the last convolutional layer "Conv2d_13_pointwise". A comparison between the "Noise Channel" under different inputs reveals that the RAW-domain classifier is adept at extracting noise patterns, effectively separating noise from the signal, which results in Grad-CAM visualizations that more closely resemble the clean input. In contrast, the RGB-domain classifier struggles to disentangle noise from the signal due to the complex non-linear processing by the Anscombe ISP, leading to significant deviations in Grad-CAM under noisy conditions and consequently to misclassification.

RAW images (RAW_{GP}) to the corresponding RGB format ($\text{RGB}_{\text{Ans-ISP}}$) for classification.

As for the Mosaic RAW method [*S1*], ImageNet images are simply mosaiced to drive RAW samples to form the $\text{simRAW}_{\text{IN}}$. Noise is then augmented onto the $\text{simRAW}_{\text{IN}}$ to train the RAW-domain classifier. Subsequently, samples in (RAW_{GP}) are tested directly.

Note that noise augmentation closely follows the studies in [*S1*] for all approaches.

B. Comparative Studies of RAW-domain Classification

Table S5 reports the image classification under low-light illumination with high noises. The proposed $\rho-Vision$ using Unpaired CycleR2R demonstrates the compellingly superior performance to the approaches, e.g., Anscombe ISP and Mosaic RAW, provided by [*S1*].

The gain of the proposed Unpaired CycleR2R to the Mosaic RAW owes the better characterization of real-life RAW images in training/devising the invISP to generate realistic simRAWs. The Mosaic RAW approach [*S1*], instead, only applies the basic mosaicking by simply neglecting the impacts of gamma correction and white balance that are vital in the transformation between RGB and RAW space..

The improvement of the Anscombe ISP to the Mosai RAW is due to the mapping between a noisy RAW image and the corresponding clean RGB sample offered by the Anscombe ISP, which significantly helps the subsequent task.

The gain of the proposed Unpaired CycleR2R to the Anscombe ISP is attributed to the better noise separation and suppression in the RAW domain. This improvement is visually corroborated in Fig. S3, where the "Noise Channel" columns under the Unpaired CycleR2R method (RAW row) exhibit a more apparent distinction between noisy and clean features. The efficacy of our model in noise modeling and separation in the RAW domain, as proofed in [*S1*], is further evidenced by the Grad-CAM visualizations. These visualizations of noisy inputs are similar to those generated from clean inputs, illustrating the model's ability to preserve essential image characteristics despite noise. In contrast, the Anscombe ISP (RGB row) reveals a significant disparity in the Grad-CAM outputs when comparing noisy and clean inputs, which may lead to classification errors.

Our Unpaired CycleR2R achieves this superior noise discrimination without increasing computational complexity, thereby maintaining the same level of FLOPs as the Mosaic RAW (lower than the Anscombe ISP).

S.V. RAW-domain Segmentation

In the main text of this paper, the detection task is successfully executed in the RAW domain with superior performance to that using the same RGB-domain model. Here we explore the feasibility of RAW-domain segmentation. Similar to the discussions in Sec. 5.2 and 6.2, we first demonstrate that the segmentation model trained with simRAW images can directly infer the segmentation cues upon the real RAW images. Second, a few-shot finetuning simRAW-pretrained segmentation model using limited labeled real RAW images further improves its performance and shows consistent gains to the model trained from scratch. Finally, ablation studies show that gamma correction is also vital for segmentation tasks in the RAW domain.

A. Datasets

Cityscapes [*S5*] is a large-scale dataset recorded in different urban streets in Europe containing 5,000 frames with high-quality pixel-level segmentation annotations. Considering the different traffic signs in China where the MultiRAW is captured, we use a communal subset including road, building, fence, traffic light, sky, person, car, truck, and bus for evaluation. Following the setup in Sec. 5.2 of the main paper, we convert the RGB samples, a.k.a RGB_{c}, into simRAW image set simRAW_{c} to train/refine RAW-domain segmentation model.

B. Training Details

We use the famous HRNetv2 [*S5*] as our segmentation network. All segmentation models are optimized by a SGD optimizer with 0.9 momentum, 5×10^{-4} weight decay and initial learning rate of 10^{-2} dropped into 10^{-4} linearly. The batch size is set as 8, and inputs are randomly cropped into 512×1024 with random flip augmentation. The experiments are conducted using an Nvidia 3090Ti GPU.

C. Comparative Studies of RAW-domain Segmentation

Table S6 and Fig. S4 compares our Unpaired CycleR2R and other methods using invISP approach [*S1*, *S1*, *S1*, *S2*] and domain-adaptation (DA) solution [*S6*, *S7*]. It can be seen that Unpaired CycleR2R outperforms the state-of-the-art CycleISP by a significant margin of $7\,\text{mIoU}$ and improves the IoU across all classes of objects. More gains are presented against other approaches.

Our model also surpasses the RGB Baseline on mIoU. Note that this RGB Baseline is prevalent in real-world applications. Such a convincing performance suggests the potential for RAW-domain segmentation. We also observe the lower IoU for some specific classes of objects between our method and the RGB Baseline. This is probably due to the optimization strategy for maximizing the overall performance but not balancing each class. This is an interesting topic for future study.

Apparently, inputting real RAW images to the RGB-domain segmentation model directly for task execution is a failure, as exemplified in the Naive Baseline, e.g., mIoU of 11.1 versus the mIoU of 47.5 in the RGB Baseline, which is due to the large discrepancy between the RGB-domain and RAW-domain models.

Implementation Friendliness. As aforementioned in Sec. 5.2, our method could generate simRAW images to train task-dependent models. However, DA-based approaches [*S1*, *S1*] designed for object detection tasks could not be applied to segmentation tasks. And DA-based segmentation methods [*S6*, *S7*] could not support the detection task either.

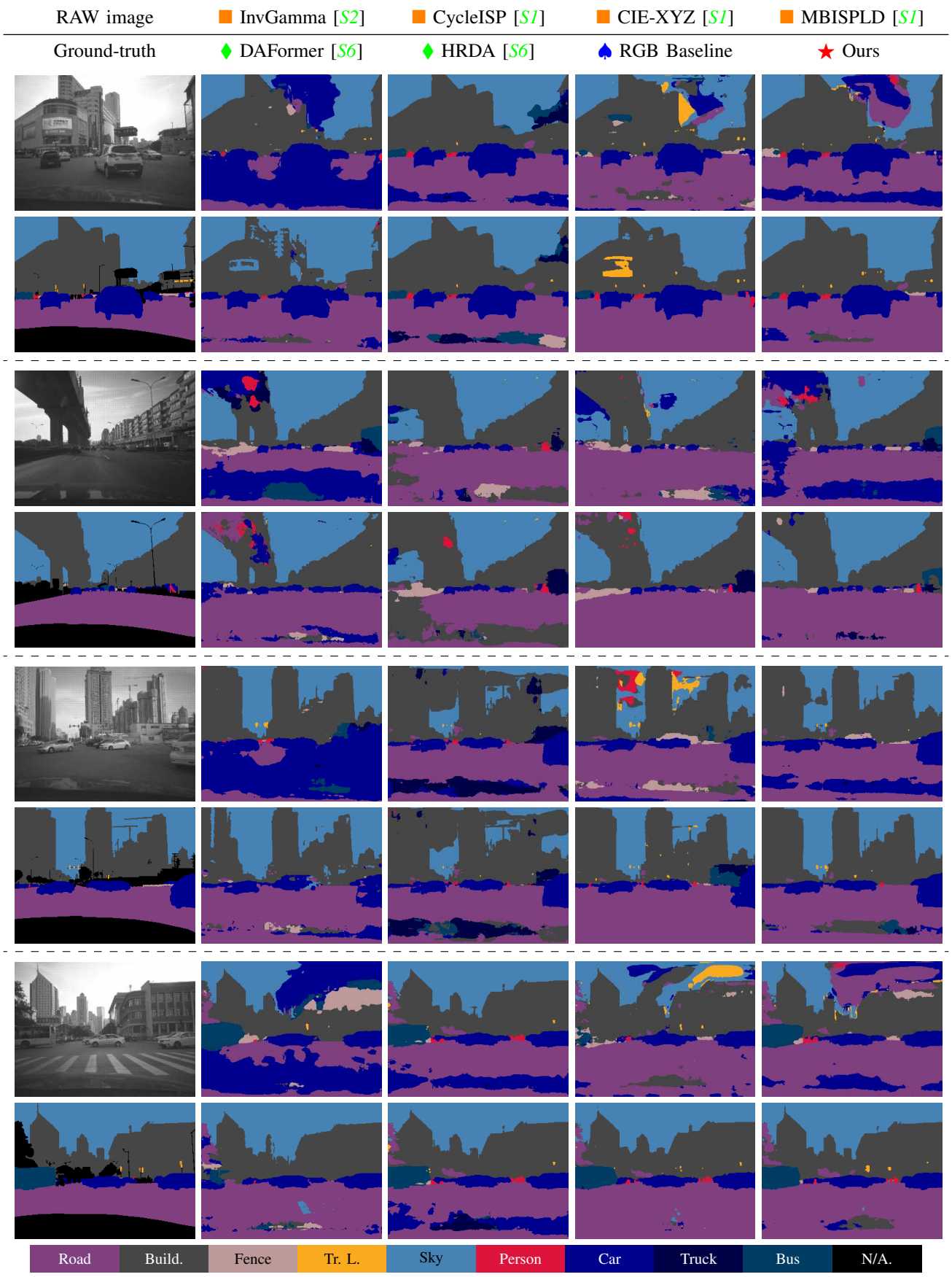

Fig. S4: **Qualitative Visualization of Pretrained RAW Segmentation Model.** Example predictions show better recognition of buildings, sky, and traffic lights by our Unpaired CycleR2R on Cityscapes RGB → iPhone RAW. Gamma correction and brightness adjustment have been applied to RAW images for a better view.

TABLE S6: **mIoU (Mean Intersection over Union) of Segmentation on the testing set of iPhone RAW images.** RGB-domain segmentation model is trained using original RGB images in *Cityscapes* [*S5*] (e.g., RGB_c); Various simRAW datasets associated with RGB_c are generated using different methods which are marked as $simRAW_c$ to train RAW-domain segmentation model. The testing RAW images in iPhone RAW RAW_i and their paired RGB images in RGB_i converted using built-in iPhone ISP are tested accordingly. HRNetv2 [*S5*] is used as the base segmentation model. ♠ Baselines, ♦ Domain Adaptation Solutions, ■ invISP Methods, ★ Ours.

Method	invISP	Segmentor		Road	Build.	Fence	Tr. L.	Sky	Person	Car	Truck	Bus	mIoU
	Train	Train	Test										
♠ Naive Baseline	-	RGB_c	RAW_i	0.3	21.6	14.8	5.7	20.7	0.4	30.0	0.4	6.2	11.1
♠ RGB Baseline	-	RGB_c	RGB_i	**89.6**	65.1	35.6	20.7	**96.1**	11.1	62.9	**21.5**	25.3	47.5
♦ DAFormer (CVPR'22) [*S6*]	-	RGB_c, RAW_i	RAW_i	75.8	49.5	15.2	1.5	90.0	5.3	58.3	0.2	6.3	32.9
♦ HRDA (ECCV'22) [*S7*]	-	RGB_c, RAW_i	RAW_i	73.8	69.1	38.5	12.3	80.6	15.0	51.2	16.2	20.9	42.0
■ InvGamma (ICIP'19) [*S2*]	RGB_i, RAW_i	$simRAW_c$	RAW_i	47.5	55.7	31.2	8.3	90.0	7.3	23.9	11.2	17.6	32.5
■ CycleISP (CVPR'20) [*S1*]	RGB_i, RAW_i	$simRAW_c$	RAW_i	84.8	63.9	35.0	18.0	86.3	9.7	55.7	18.0	20.6	43.6
■ CIE-XYZ Net (TPAMI'21) [*S1*]	RGB_i, RAW_i	$simRAW_c$	RAW_i	78.7	64.4	36.7	3.0	84.2	5.4	48.6	2.3	15.4	37.6
■ MBISPLD (AAAI'22) [*S1*]	RGB_i, RAW_i	$simRAW_c$	RAW_i	72.5	60.8	39.4	7.3	78.6	13.3	41.0	17.7	20.8	39.0
★ **Unpaired CycleR2R**	RGB_c, RAW_i	$simRAW_c$	RAW_i	88.9	**70.5**	**40.9**	**24.7**	95.5	**21.4**	**64.3**	19.1	**30.0**	**50.6**

Build. ← Building; **Tr. L.** ← Traffic Light.

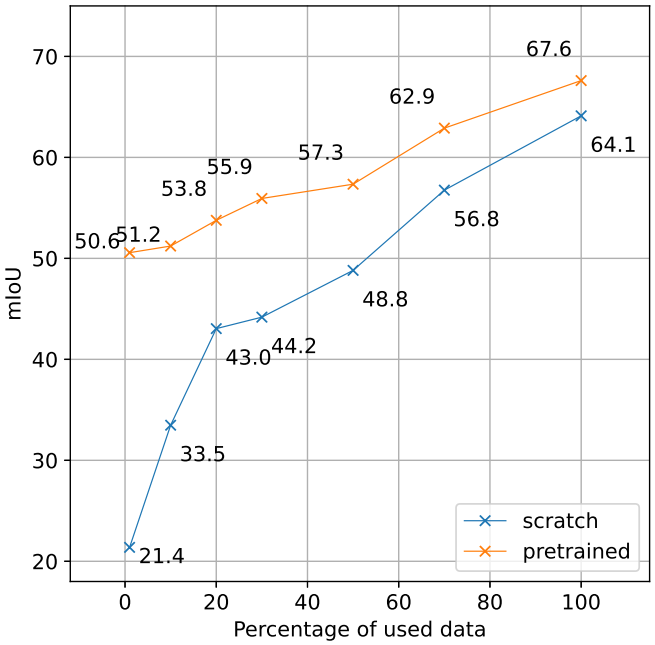

Fig. S5: **Few-shot finetuning using limited camera RAWs.** The simRAW-pretrained HRNetv2 [*S5*] is obtained by using samples in $simRAW_c$ generated by our Unpaired CycleR2R, which is then finetuned using limited camera RAW images; and the "scratch" model is randomly initialized and then trained using the same number of labeled real RAW images.

D. Comparative Studies of Few-Shot Finetuning

The performance of the simRAW-pretrained segmentation model could be further boosted by feeding more real labeled RAW images. We further finetune our segmentation model using our MultiRAW dataset (iPhone XSmax) with all classes. As depicted in Fig. S5, the segmentation accuracy is improved and consistently outperforms the scratch model which is initialized randomly and then trained using the same labeled real RAW images.

S.VI. Extra Quantitative Visualization

In Fig. S6, we present a visual comparison between our simulated RAW images and real RAW images. We also offer more qualitative visualizations of our lossy RIC at low Bits-rate and high Bits-rate in Fig. S7 and Fig. S8 respectively. Similar to the results in the main content of this work, we can clearly observe the subjective improvements of the proposed lossy RIC compared to the HEVC and VVC. Especially for the traffic light and car information, our lossy RIC provides sharper and less noisy reconstructions closer to the ground truth samples. Also, we give visualizations of progressive decoding using our lossless RIC within various cameras in Fig. S9-S11. Our lossless RIC could provide low-resolution previews for different cameras (iPhone XSmax, Huawei P30pro, and asi 294mcpro) and different scenes (both daylight and nighttime), which is helpful for professional photography and network transmission.

References

[*S1*] S. Diamond, V. Sitzmann, F. Julca-Aguilar, S. Boyd, G. Wetzstein, and F. Heide, "Dirty pixels: Towards end-to-end image processing and perception," *ACM Transactions on Graphics (TOG)*, vol. 40, no. 3, pp. 1–15, 2021. 3, 4, 5, 6, 7

[*S2*] R. R. Selvaraju, M. Cogswell, A. Das, R. Vedantam, D. Parikh, and D. Batra, "Grad-cam: Visual explanations from deep networks via gradient-based localization," in *Proceedings of the IEEE international conference on computer vision*, 2017, pp. 618–626. 6

[*S3*] J. Deng, W. Dong, R. Socher, L.-J. Li, K. Li, and L. Fei-Fei, "Imagenet: A large-scale hierarchical image database," in *2009 IEEE conference on computer vision and pattern recognition*. Ieee, 2009, pp. 248–255. 5

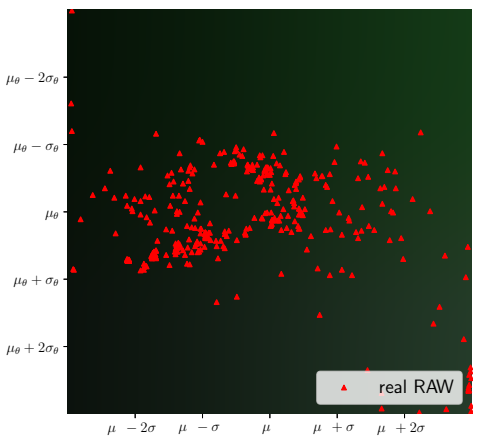

(a) simRAW is a superset of real RAW data

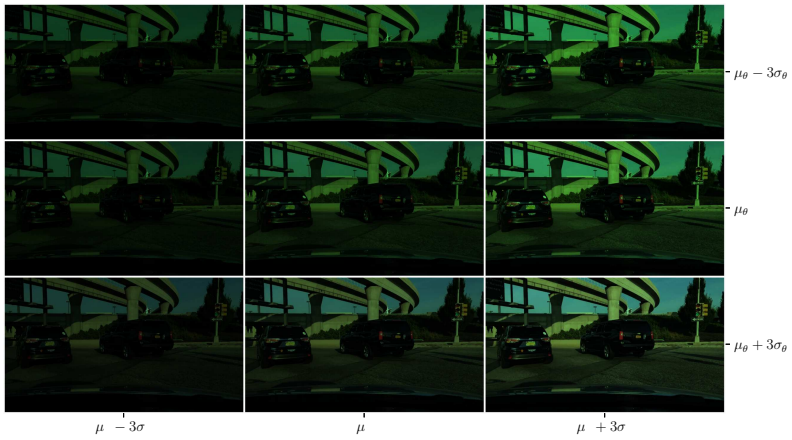

(b) simRAW examples

(c) Testing RGB

(d) Random real RAW images from multiRAW dataset

(e) simRAW w/o IEM

(f) simulating RAW images by injecting noise to $E^{-1}(\cdot)$ outputs w/o using IEM

Fig. S6: **Evaluation of the Illumination Estimation Module (IEM).** *Demosaicing has been applied to all images to enhance visibility.* (a) Adapting IEM to generate the simRAW's coverage using the mean color, where the color of each point ϕ_i, θ_j represents the average color of a simRAW generated by sampled illumination parameters ϕ_i, θ_j. In contrast, red markers indicate the average color of real RAW images. It clearly reveals that adapting IEM can cover all real-world illumination conditions in real RAW data. (b) simRAW examples generated by our Unpaired CycleR2R with various ϕ, θ, illustrating the IEM's ability to produce a wide range of illumination variations. (c) The corresponding RGB image fed into the invISP of our Unpaired CycleR2R, which is from the BDD100K dataset. (d) Random real RAW images from the multiRAW dataset, displaying the natural variability in illumination and color temperature. (e) Simulating a RAW image without using IEM, which can only produce a single simRAW per RGB input due to the absence of probabilistic illumination estimation. (f) Simulating RAW images by injecting noise to $E^{-1}(\cdot)$ outputs, which can produce multiple simRAW samples without requiring IEM but demonstrate unrealistic diversity induction in RAW Images. $E^{-1}(\cdot)$ is defined in invISP (see Fig. 2 in the main paper).

[*S4*] A. G. Howard, M. Zhu, B. Chen, D. Kalenichenko, W. Wang, T. Weyand, M. Andreetto, and H. Adam, "Mobilenets: Efficient convolutional neural networks for mobile vision applications," *arXiv preprint arXiv:1704.04861*, 2017. 5

[*S5*] M. Cordts, M. Omran, S. Ramos, T. Rehfeld, M. Enzweiler, R. Benenson, U. Franke, S. Roth, and B. Schiele, "The cityscapes dataset for semantic urban scene understanding," in *Proc. of the IEEE Conference on Computer Vision and Pattern Recognition (CVPR)*, 2016. 7, 9

[*S6*] L. Hoyer, D. Dai, and L. Van Gool, "Daformer: Improving network architectures and training strategies for domain-adaptive semantic segmentation," in *Proceedings of the IEEE/CVF Conference on Computer Vision and Pattern Recognition*, 2022, pp. 9924–9935. 7, 8, 9

[*S7*] ——, "Hrda: Context-aware high-resolution domain-adaptive semantic segmentation," *arXiv preprint arXiv:2204.13132*, 2022. 7, 9

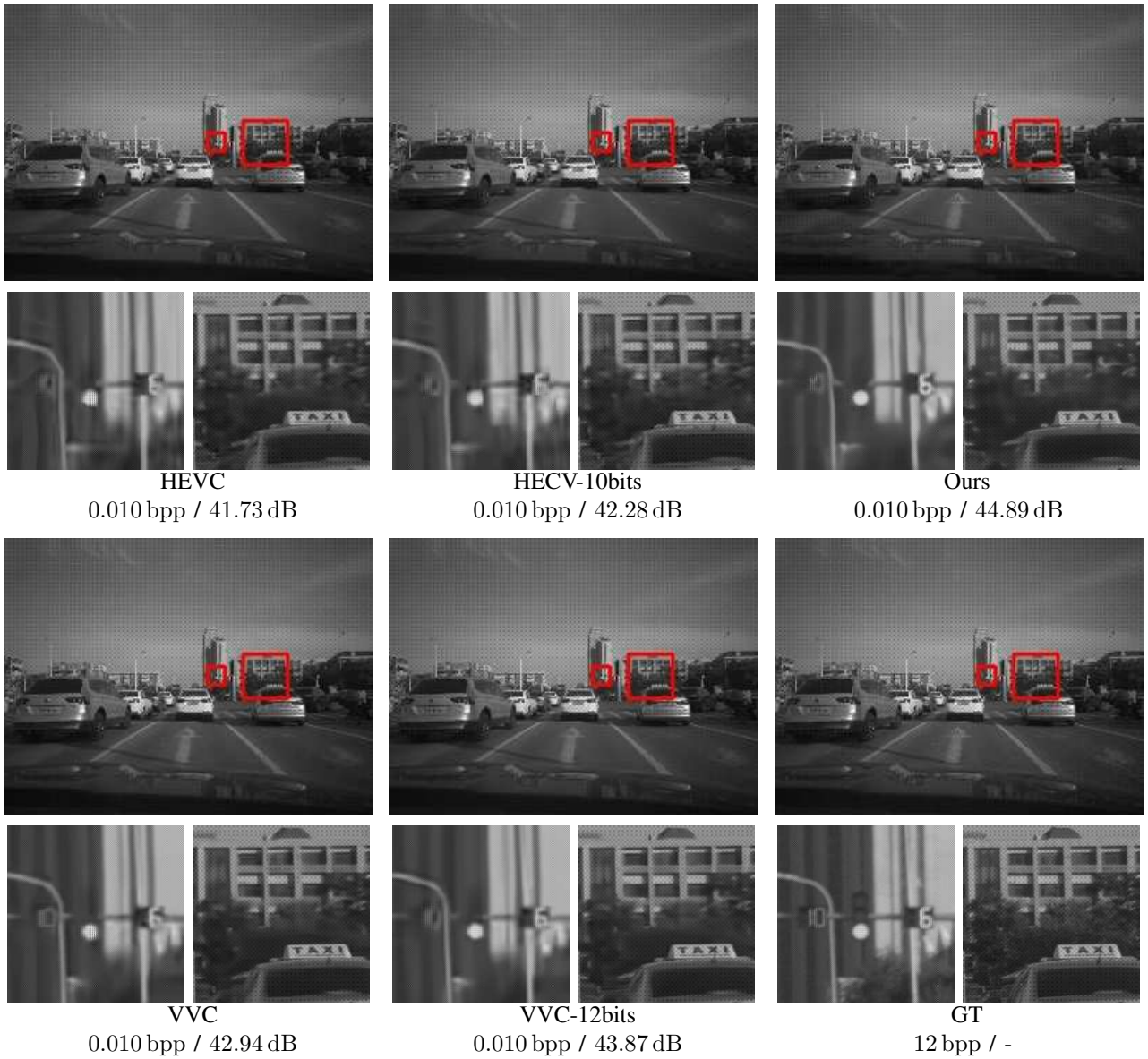

Fig. S7: **Qualitative Visualization of Lossy RIC at Low Bits-rate.** Reconstructions and close-ups of the HEVC, VVC, and our method. Corresponding bpp and PSNR are marked. Gamma correction and brightness adjustment have been applied for a better view. *Zoom for better details.*

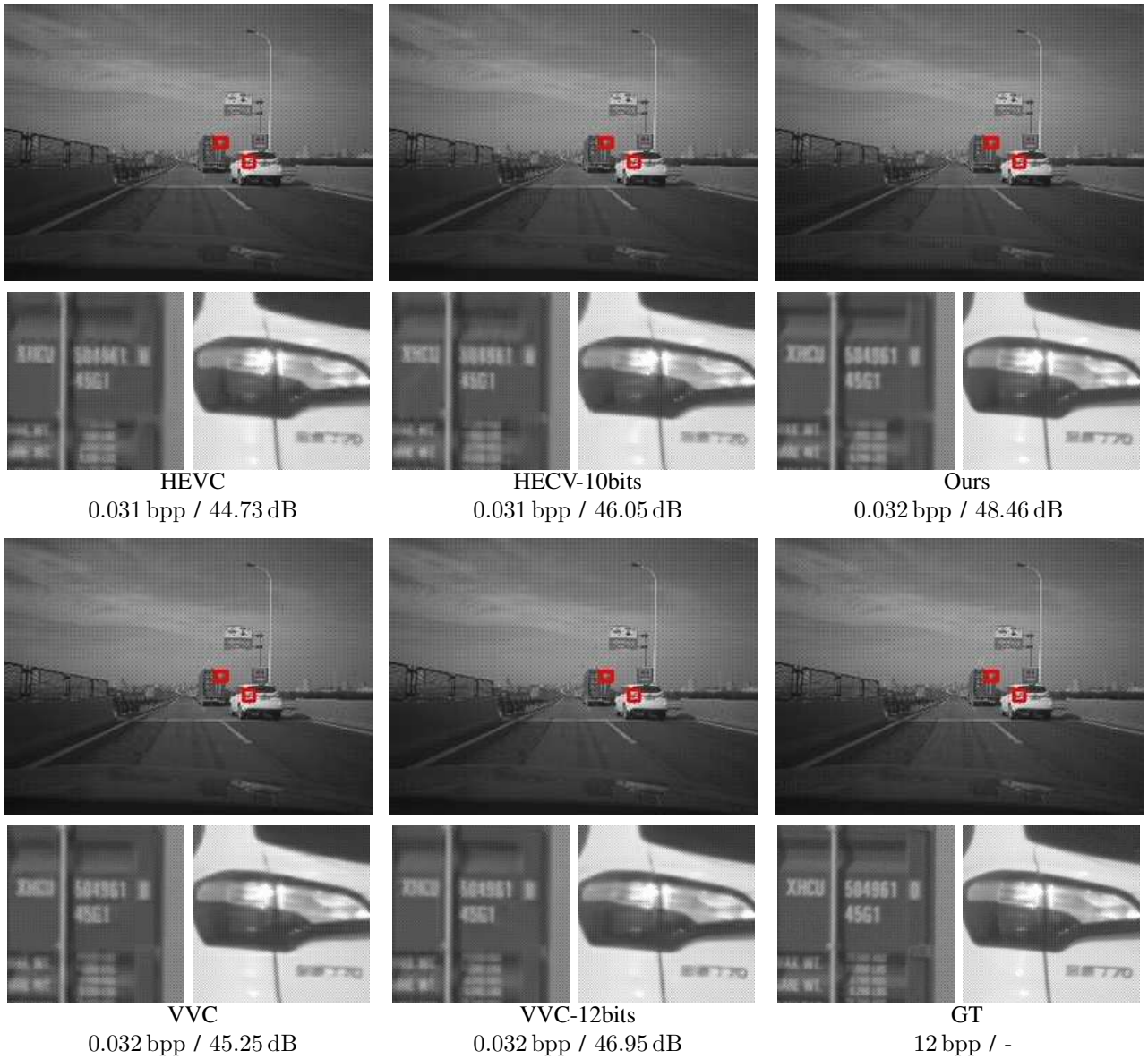

Fig. S8: **Qualitative Visualization of Lossy RIC at High Bits-rate.** Reconstructions and close-ups of the HEVC, VVC, and our method. Corresponding bpp and PSNR are marked. Gamma correction and brightness adjustment have been applied for a better view. *Zoom for better details.*

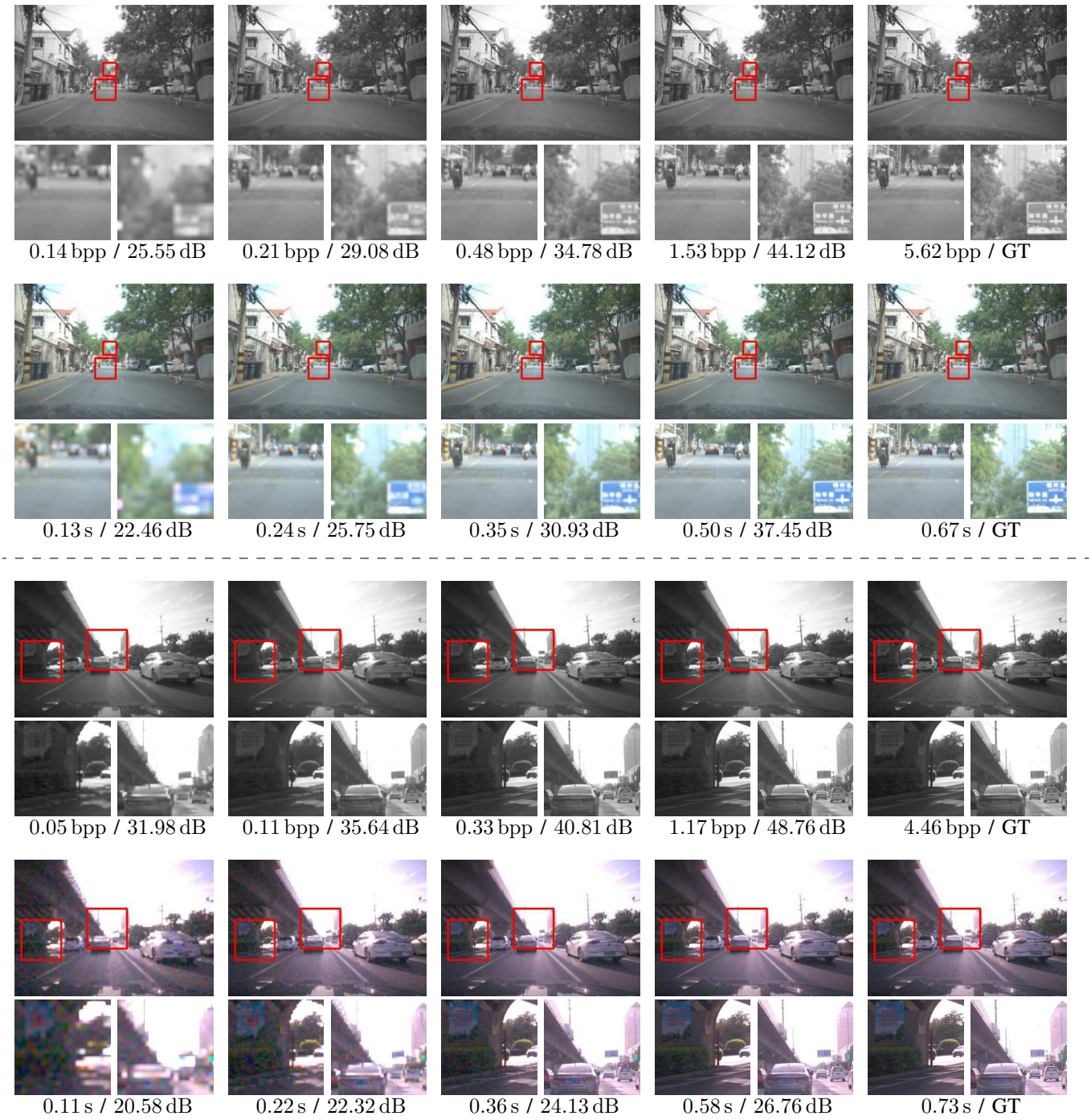

Fig. S9: **Qualitative Visualization of Lossless RIC Progressive Decoding (iPhone XSmax).** The gradual reconstruction of RAW images and their corresponding RGB images converted by an in-camera ISP. Bits per pixel (bpp) / PSNR (dB) is shown under RAW images. Decoding latency (s) / PSNR (dB) is also listed below RGB images. PSNR is derived against the GT (ground truth). Gamma correction and brightness adjustment have been applied for a better view. *Zoom for more details.*

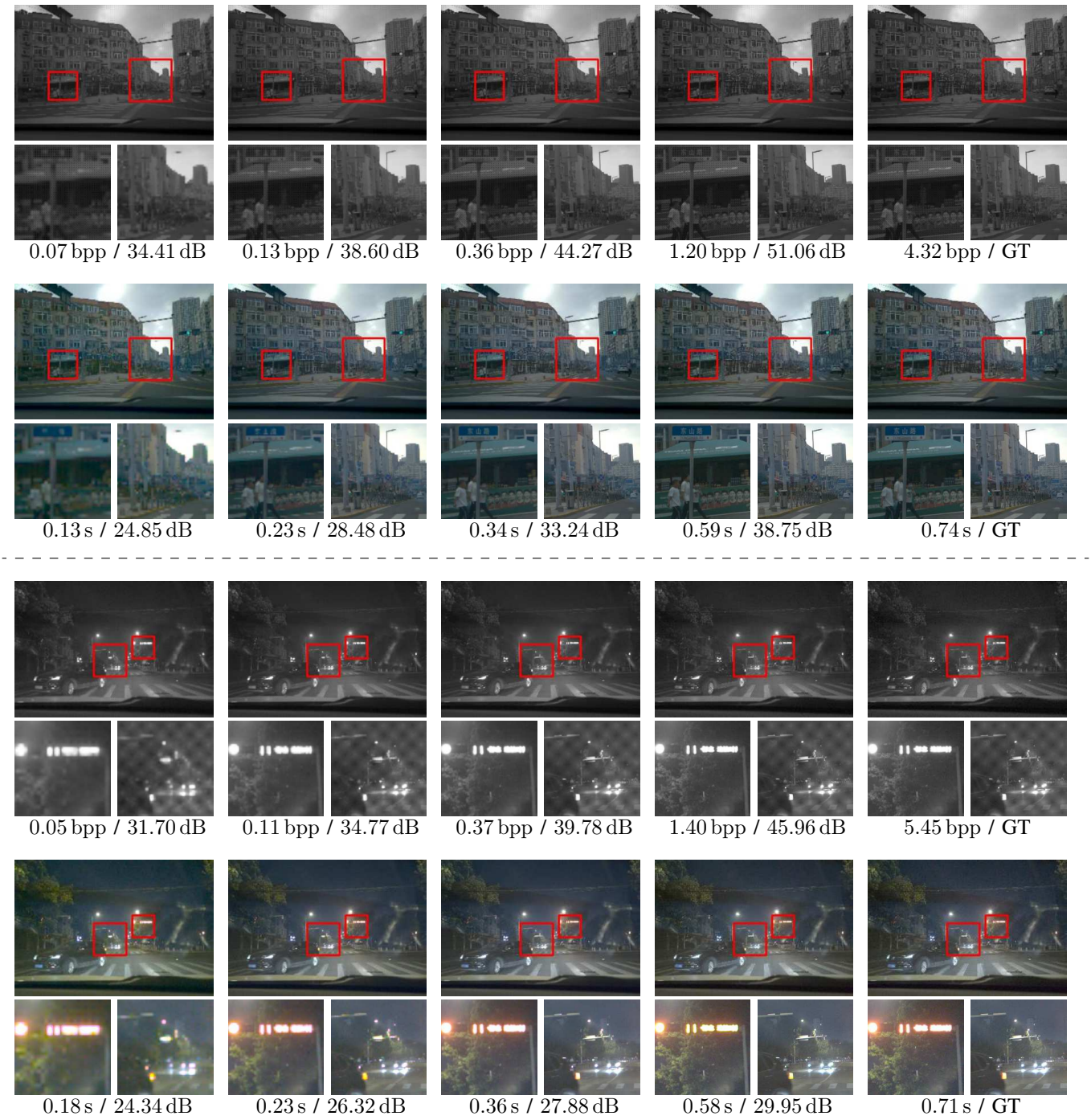

Fig. S10: **Qualitative Visualization of Lossless RIC Progressive Decoding (Huawei P30pro).** The gradual reconstruction of RAW images and their corresponding RGB images converted by an in-camera ISP. Bits per pixel (bpp) / PSNR (dB) is shown under RAW images. Decoding latency (s) / PSNR (dB) is also listed below RGB images. PSNR is derived against the GT (ground truth). Gamma correction and brightness adjustment have been applied for a better view. *Zoom for more details.*

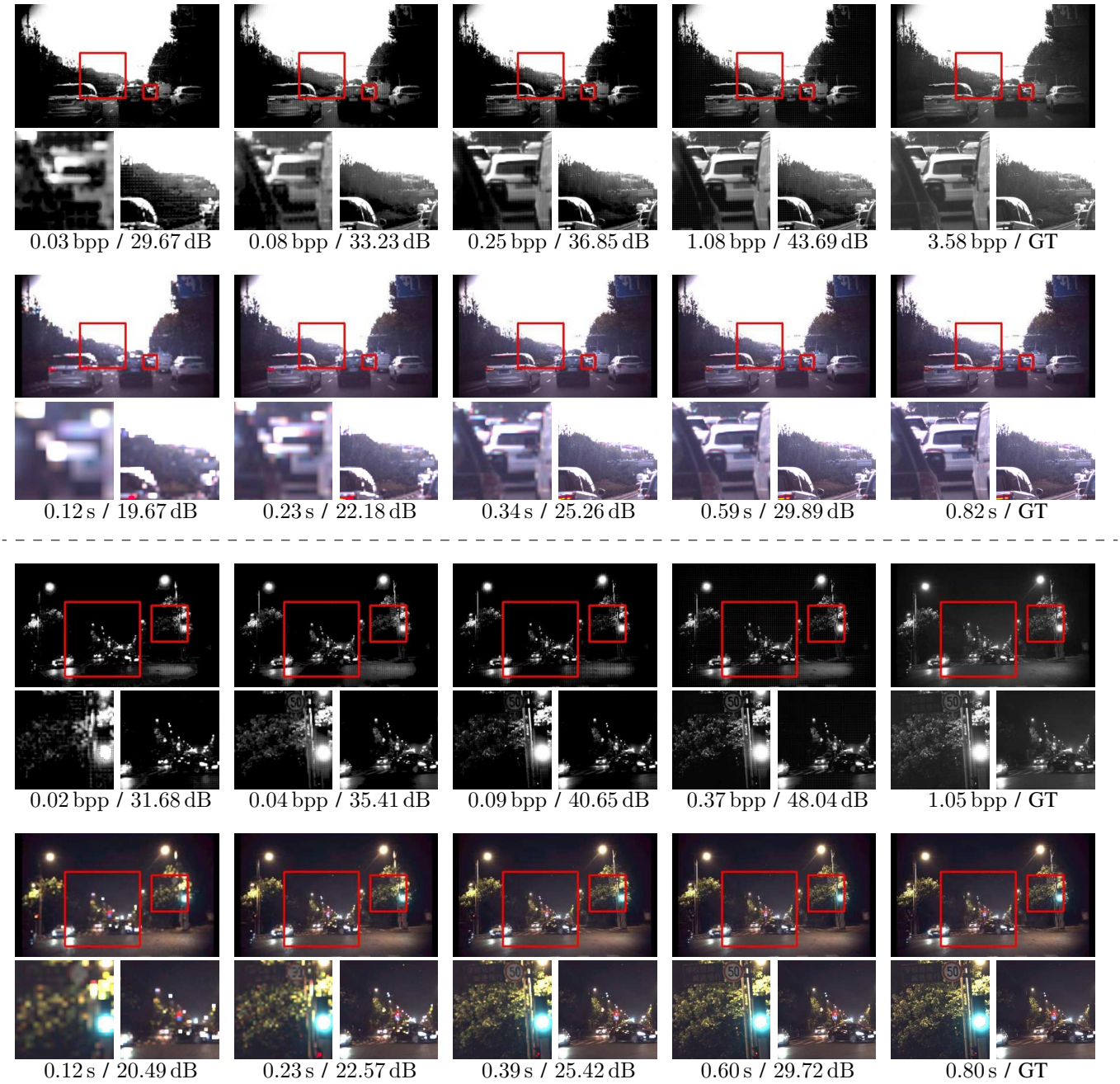

Fig. S11: **Qualitative Visualization of Lossless RIC Progressive Decoding (asi 294mcpro).** The gradual reconstruction of RAW images and their corresponding RGB images converted by an in-camera ISP. Bits per pixel (bpp) / PSNR (dB) is shown under RAW images. Decoding latency (s) / PSNR (dB) is also listed below RGB images. PSNR is derived against the GT (ground truth). Gamma correction and brightness adjustment have been applied for a better view. *Zoom for more details.*